Protein thiol alterations drive pathologic liquid-liquid phase separation in the aging brain

Thibaut Vignane[1,20], Martín Hugo[1,21], Polina Reichert,[2] Christian Hoffmann[3], Antonia Katsouda[4,5], Davide D'Andrea,[2] Han Wang[3], Johannes V. Tromm,[3] Marko Miler[1], Ferran Comas[1], Dunja Petrovic[1], Suyuan Chen[1], Jan Lj. Miljkovic[6], Danail Stoychev,[2] Erik Lacko,[2] Vladimir M. Jovanovic,[7] Suwarna Chakraborty,[8] Sunil J. Tripathi,[8] Edwin Vázquez-Rosa,[9,10,11,12] Jordan L. Morris,[6] Suvagata Roy Chowdhury,[6] Julien Prudent,[6] Albert Sickmann,[1] Natalija Polovic,[13] Andrew A. Pieper,[9,10,11,12,14,15] Ilan Davis,[2] Kostas Tokatlidis,[2] Bindu D. Paul,[8,16,17,18] Michael P. Murphy[6,19], Christian Munch,[20] Andreas Papapetropoulos[4,5], Dragomir Milovanovic[3], Milos R. Filipovic[1,2*]

Affiliations:

[1]Leibniz Institute for Analytical Sciences, ISAS, e.V. Dortmund, Germany

[2]School of Molecular Biosciences, MVLS College, University of Glasgow, UK

[3]Laboratory of Molecular Neuroscience, German Center for Neurodegenerative Diseases, Berlin, Germany

[4]Clinical, Experimental Surgery and Translational Research Center, Biomedical Research Foundation of the Academy of Athens, Athens, Greece

[5]Laboratory of Pharmacology, Department of Pharmacy, National and Kapodistrian University of Athens, Athens, Greece

[6]MRC Mitochondrial Biology Unit, University of Cambridge, Keith Peters Building, CB2 0XY, UK

[7]Bioinformatics Solution Center, Institute for Informatics, Freie Universität Berlin, Berlin, Germany

[8]Department of Pharmacology and Molecular Sciences, Johns Hopkins University School of Medicine, Baltimore, MD, USA.

[9]Department of Psychiatry, Case Western Reserve University, Cleveland, OH, USA.

[10]Brain Health Medicines Center, Harrington Discovery Institute, University Hospitals Cleveland Medical Center, Cleveland, OH, USA.

[11]Geriatric Psychiatry, GRECC, Louis Stokes Cleveland VA Medical Center, Cleveland, OH, USA.

[12]Institute for Transformative Molecular Medicine, School of Medicine, Case Western Reserve University, Cleveland, OH, USA.

[13]Department of Biochemistry, Faculty of Chemistry, University of Belgrade, Belgrade, Serbia

[14]Department of Pathology, Case Western Reserve University, School of Medicine, Cleveland, OH, USA.

[15]Department of Neurosciences, Case Western Reserve University, School of Medicine, Cleveland, OH, USA

[16]The Solomon H. Snyder Department of Neuroscience, Johns Hopkins University School of Medicine, Baltimore, MD 21205, USA.

[17]Department of Psychiatry and Behavioral Sciences, Johns Hopkins University School of Medicine, Baltimore, MD 21205, USA.

[18]Lieber Institute for Brain Development, Baltimore, MD 21205, USA.

[19]Department of Medicine, University of Cambridge, Cambridge, CB2 0QQ, United Kingdom

[20]Institute of Molecular Systems Medicine, University Hospital Frankfurt Goethe University Frankfurt, Germany,

[21]Current address: Serra Húnter Fellow, Departament de Bioquimica i Biologia Molecular, Universitat Autònoma de Barcelona, Bellaterra, 08193 Barcelona, Spain.

*Corresponding author.

Email: milos.filipovic@glasgow.ac.uk

Cellular homeostasis relies on the precise regulation of chemical processes, including protein posttranslational modifications (PTMs) and biomolecular condensation. Aging disrupts the equilibrium of these processes, increasing susceptibility to disease and mortality. Using advanced chemoproteomic techniques, we investigated cysteine PTMs in the aging mouse brain and generated web-based explorer (https://aging-redox-proteomics-viewer.streamlit.app/). Our findings reveal that age-related increases in thiol oxidation promote the formation of biomolecular condensates. In contrast, protein persulfidation, regulated by endogenous hydrogen sulfide (H_2S) production, inhibits biomolecular condensation, thereby preserving protein function. These cysteine PTMs significantly alter the phase separation properties of synapsin 1, a key regulator of synaptic activity, contributing to impaired neurotransmitter release associated with aging and neurodegenerative diseases. Age-induced alterations in cysteine PTMs influence the phase separation properties of synapsin 1 and G3BP2, leading to impaired neurotransmitter release and defective stress-granule formation/resolution, respectively, both features associated with aging and neurodegenerative diseases. Mice deficient in cystathionine γ-lyase, the enzyme responsible for H_2S production and protein persulfidation, exhibit reduced lifespans and spontaneously develop neurofibrillary tangles and protein aggregates with age. Our results highlight the therapeutic potential of protein persulfidation in reversing dysregulated biomolecular condensation, offering new avenues for using sulfide donors to mitigate age-related diseases.

Introduction

Aging is characterized as a progressive decline in physiologic fitness, driven by the accumulation of both random and deterministic deleterious changes.[1] The redox chemistry of the sulfur-containing amino acid cysteine[2] positions it as a key target for age-related modifications and a critical component of cellular defense against oxidative damage.[3] Recent studies suggest that cysteine persulfidation (PSSH), an evolutionarily conserved posttranslational modification (PTM) of proteins mediated by the gasotransmitter hydrogen sulfide (H_2S), may protect proteins from excessive oxidation and functional loss (Fig. 1a).[4] Cystathionine γ-lyase (CSE; gene name: *CTH*), is a key enzyme in H_2S production that regulates PSSH levels[4,5] and has been recently proposed as one of conserved pro-longevity genes in RNA-seq analyses of lifespan-extending interventions in mice.[6,7] This is particularly relevant in the aging brain, where reduced CSE expression is associated with neurodegenerative diseases.[8–10] Restoring PSSH levels has been shown to extend lifespan, improve healthspan[11] and mitigate cognitive decline associated with Alzheimer disease (AD).[8] However, the traditional view that cysteine modifications primarily only affect protein function may not fully capture their biological impact. Indeed, emerging evidence suggests that protein function can also be regulated through intracellular phase transitions into membraneless compartments, a process known as liquid-liquid phase separation (LLPS).[12,13] Here, we hypothesize that the age-induced switch from PSSH towards cysteine oxidation to sulfenic (PSOH) and finally sulfonic acid (PSO_3H) affects the ability of proteins to phase separate and promote their aggregation (Fig. 1a). Such changes may impose additional stress on aging cells, driving them toward pathophysiological states.

Main

Aging is associated with a proteome-wide increase of PSOH and decrease in PSSH

Conventional methods for detecting thiol oxidation[14] often fail to differentiate between PSOH and PSSH,[15] as both modifications are oxidative in nature and intrinsically interconnected, despite their distinct biological roles.[2,4,16,17] These modifications are highly reactive and short-lived, necessitating the use of selective labeling techniques to accurately assess their dynamics (Supplementary text). To investigate the impact of aging on thiol oxidation, we applied selective chemoproteomic approaches for

global detection of PSOH and PSSH[4,18] in the frontotemporal region of mouse brain at 10 weeks, 10 months, and 18 months of age (Fig. 1b). We focused on the frontotemporal region because it is particularly vulnerable to age-associated neurodegeneration and exhibits early molecular changes relevant to cognitive decline.

Sulfenylated proteins were identified across most cellular compartments (Fig. 1c). Although PSOH is considered a transient modification and an early step in thiol oxidation with multiple fates (Fig. 1a), we surprisingly observed a steady, age-dependent increase in sulfenylated protein levels (Fig. 1d, Extended Data Fig. 1a-c, Supplementary Table 1). Principal components analysis (PCA) revealed clear separation between the sulfenylomes of young and old mice (Extended Data Fig. 1d). Notably, a recent study demonstrated that the benzothiazine-based chemoselective probe (BTD) is highly specific for PSOH, with no side-reactivities.[19] Leveraging this, we opted for total protein enrichment, identifying a significantly higher number of endogenously sulfenylated proteins (Fig. 1e), compared to previous reports that used site-centric peptide enrichment.[18,20]

Proteins with significantly elevated PSOH levels in aging were primarily associated with metabolic processes and protein translation, folding, localization and transport, as well as regulation of phosphorylation, synaptic transmission, response to stimuli, actin and cytoskeleton organization, and neuronal development (Fig. 1f, Extended Data Fig. 1e, Supplementary Table 1). To discern age-dependent patterns, we clustered proteins using the fuzzy c-means method. Approximately 20% of sulfenylated proteins exhibited significant changes (FDR adjusted p value ≤ 0.05) in PSOH levels with age, with about half showing a continuous age-dependent increase (Fig. 1g). These proteins were enriched in critical neuronal pathways (e.g. synaptic vesicle cycle, carbon metabolism, proteasome) and highly implicated in neurodegenerative diseases (amyotrophic lateral sclerosis, Parkinson's disease, spinocerebellar ataxia, Huntington's disease) (Fig. 1h).

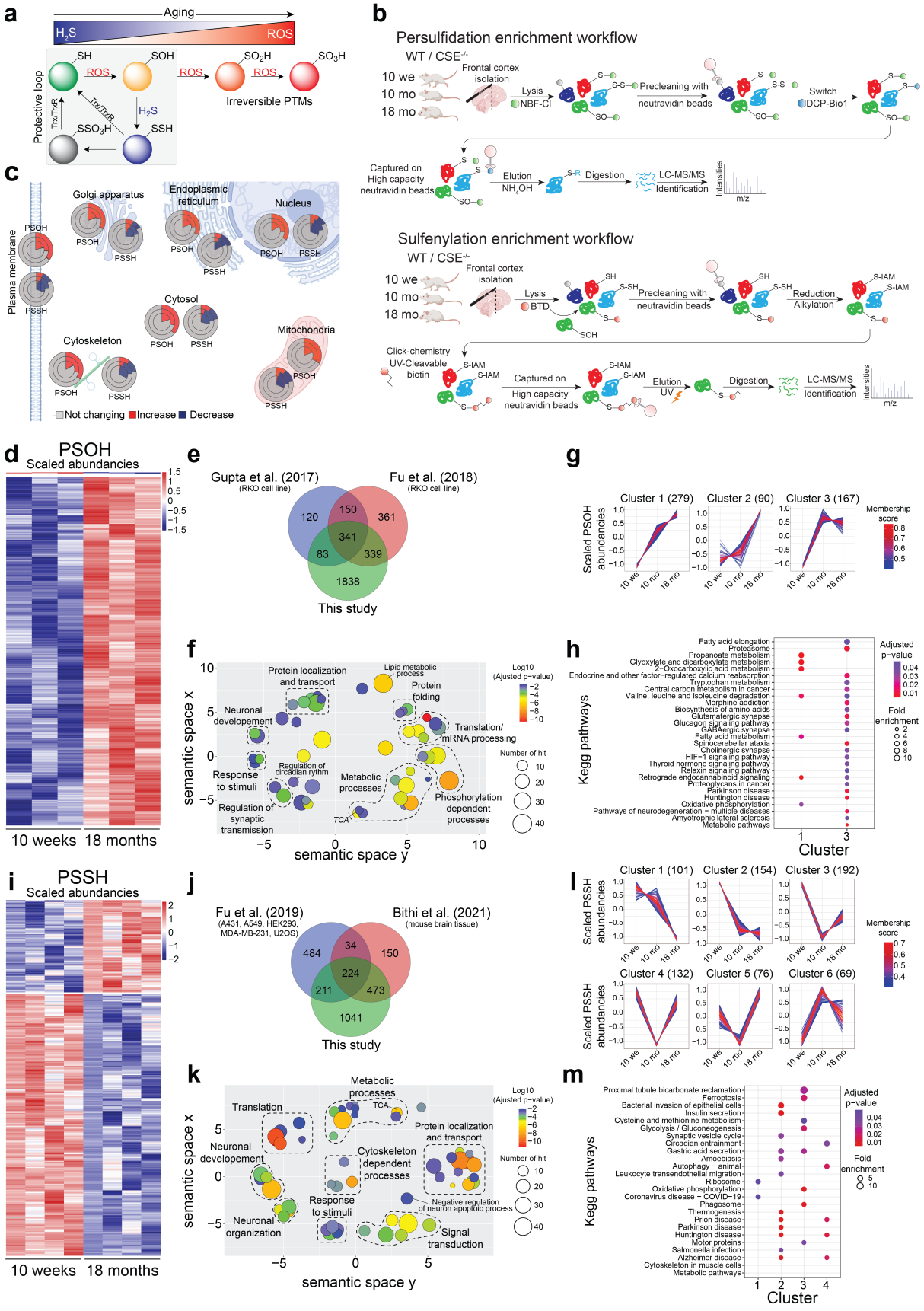


Figure 1. Chemoproteomic analysis of protein sulfenylation and persulfidation reveals substantial alteration of cysteine modifications in aging. (**a**) Protective persulfidation loop prevents cysteine hyperoxidation. (**b**) Chemoproteomic workflows of PSOH and PSSH

detection. The PSSH workflow is based on Zivanovic et al, 2019,[4] while the PSOH workflow is adapted from Fu et al, 2018.[18] (**c**) PSOH and PSSH changes in subcellular compartments. From inside to outside, circles indicate changes in 10-month-old, 18-month-old wild type mice and 10-week-old *Cse*$^{-/-}$ mice compared to 10-week-old wild type animals, respectively. Color denotes the type of change with red showing significant increase, blue significant decrease while grey represents the proportion of proteins in which the cysteine modification is not changing. Protein subcellular localization was determined using QuickGO platform and GO slims annotations.[21] Proteins with multiple localization were also included in presentation. (**d**) Heatmap showing the significant changes of PSOH in 18-month-old mice compared to 10-week-old mice (n = 3; FDR adjusted p value ≤ 0.05). (**e**) Venn diagram comparing the sulfenylated proteins identified within our study against two other data sets, Fu et al, 2018[18] and Gupta et al, 2017.[20] (**f**) GO term enrichment (biological process) of the proteins showing significant PSOH increase (FDR adjusted p value ≤ 0.05) at least once across the age. Enrichment was done using DAVID[22,23] and the outcomes visualized through REVIGO.[24] Significant GO terms passed the Benjamini adjusted p-value threshold of 0.01. Circle dimensions correspond to the protein count within specific GO terms and color gradients to the significance. (**g**) Hierarchical cluster analysis of the proteins with PSOH levels significantly changing (FDR adjusted p value ≤ 0.05) at least once in all 3 ages based on trend profile. (**h**) KEGG pathway enrichment analysis was applied for each cluster shown in (**g**). Benjamini adjusted p-value was used to filter for significant enrichment. (**i**) Heatmap showing the significant changes of PSSH in 18-month-old mice compared to 10-week-old mice (n = 4, FDR adjusted p value ≤ 0.05). (**j**) Venn diagram comparing the persulfidated proteins identified within our study against two other data sets, Fu et al, 2019,[25] and Bithi et al, 2021.[5] (**k**) GO term enrichment (biological process) of the proteins showing significant decrease of PSSH at least once in all 3 ages based on trend profile. (**l**) Hierarchical clustering of the proteins for which persulfidation was found to be changing at least once in all 3 ages (FDR adjusted p value ≤ 0.05), into 6 different groups based on the trend profile. (**m**) Corresponding KEGG pathway enrichment analysis for the clusters shown in (**l**). Benjamini adjusted p-value was used to filter for significant enrichment.

To exclude the possibility that these changes stemmed from variations in protein expression, we performed label-free quantitative proteomic analysis on the same samples (Supplementary Fig. 1, Supplementary Table 2). While aging did affect the brain proteome to some extent (Supplementary Fig. 1), consistent with previous reports,[26] the observed changes in sulfenylation were not attributable to alterations in protein expression (Extended Data Fig. 1f,g). Specifically, plotting sulfenylome changes against total proteome changes showed minimal scattering, with only a few PSOH targets following protein expression trends (Extended Data Fig. 1f,g). These findings indicate that the age-related increase in steady-state PSOH levels (Fig. 1d) reflects heightened oxidative stress in the aging brain, which is further supported by changes in the levels of key antioxidant enzymes (Extended Data Fig. 2).

In contrast, PSSH levels predominantly decreased with age, albeit non-linearly (Fig. 1i, Extended Data Fig. 3a-c, Supplementary Table 3). We identified nearly 2000 endogenously persulfidated proteins, doubling the number previously reported using

alternative labeling methods (Fig. 1j).[5,25,27] Although dimedone-based probes can exhibit minor side reactions with highly reactive amino groups,[19] the dimedone-switch method for persulfide labeling includes a blocking step with 4-chloro-7-nitrobenzofurazan (NBF-Cl),[4] eliminating this possibility. Additionally, a pre-cleaning step with neutravidin beads ensures the removal of endogenously biotinylated proteins, leaving only those selectively labelled for PSSH (Fig. 1b).[4]

Similar to sulfenylation, persulfidated proteins were distributed across most cellular compartments (Fig. 1c) and involved in diverse processes, including metabolism, protein translation, localization, and transport, response to stimuli, signal transduction, and neuronal development and organization (Fig. 1k, Extended Data Fig. 3e). PCA of persulfidomes showed clear separation between age groups (Extended Data Fig. 3d). Approximately 40% of persulfidated proteins showed significant changes at one or more age points (Fig. 1l). Unlike the linear or plateauing increase observed for sulfenylation (Fig. 1g), persulfidation followed a more complex pattern, with mid-aged mice showing the most consistent decline (~80% across 5 of 6 clusters, Fig. 1l). However, some proteins exhibited partial recovery in PSSH levels by 18 months (clusters 3-5, Fig. 1l). The pathways particularly enriched in those clusters are the ones controlling circadian rhythmicity and autophagy, as well as different neurodegenerative diseases (cluster 4). This mid-life decline aligns with recent reports of non-linear dynamics of multi-omics profiles in human aging.[28]

These observations are also consistent with the cellular distribution of sulfide-producing enzymes: CSE is localized to neurons, cystathionine beta synthase (CBS) to glial cells, and 3-mercaptopyruvate sulfurtransferase (MPST) to both neurons and astrocytes.[4] Thus, the observed changes in persulfidation reflect cumulative effects across cell types. However, it is the loss of CSE-regulated persulfidation that has profound implications for aging and neurodegeneration, as its depletion shifts the balance toward neurodegenerative events (Chakraborty et al, 2025, accompanying study).

The proteins showing age-related PSSH decline were particularly enriched in components of ribosomes, insulin secretion, synaptic vesicle cycle, and neurodegenerative diseases, while proteins showing decline and partial recovery were associated with ferroptosis, cysteine and methionine metabolism, oxidative phosphorylation, and autophagy (Fig. 1m). Importantly, changes in the total proteome

did not significantly affect the observed age-related decline in PSSH (Extended Data Fig. 3f-g). An ~ 37 % overlap between proteins found to change their PSOH and PSSH with aging is observed (Extended Data Fig. 3h) with majority of those showing a decline of PSSH and an increase of PSOH (Extend Data Fig. 3i,j), in agreement with reduced transsulfuration pathway and increased ROS observed in aging. To make this complex data analysis easily accessible, we generated an interactive platform that allows comparison across different PTMs and ages and integrates protein search with pathway visualization (https://aging-redox-proteomics-viewer.streamlit.app/).

CSE is a key regulator of the PSOH to PSSH switch in the aging brain

Recent studies have highlighted the critical role of CSE-derived H_2S and subsequent protein persulfidation in lifespan-extending interventions such as dietary restriction.[4,5,29] CSE has been identified as a pro-longevity gene in studies using lifespan-extending interventions in mice.[6,7] In the brain, reduced CSE expression is associated with neurodegenerative conditions, including AD and spinocerebellar ataxia,[3,8,10] and mice lacking CSE exhibit a Huntington disease-like phenotype.[9,30]

Further analysis of aging mouse brain metabolome[31] and transcriptome[32] datasets confirms that *Cth* expression decreases in the cerebral cortex of aged mice, leading to the accumulation of its substrates, such as homocysteine and cysteine (Supplementary Fig. 2a and 3). Similarly, a significant age-related decline of *CTH* mRNA expression (both isoforms 1 and 2) is observed in the human frontal cortex of both sexes[33] (Supplementary Fig. 2b,c). In contrast, no significant age-related changes were detected in the expression of *Mpst* or *Cbs* in aging mice (Supplementary Fig. 2a). However, we did observe a notable increase in their expression in the aging human brain (Supplementary Fig. 2d).

To investigate how CSE-derived H_2S modulates thiol remodeling at the proteome level, we compared PSOH and PSSH levels between wild type (WT) and Cse knockout ($Cse^{-/-}$) mice (Supplementary Table 4). Significantly higher PSOH levels were observed in the brains of 10-week-old $Cse^{-/-}$ mice compared to their WT littermates (Fig. 2a, Extended Data Fig. 4a,b). Notably, approximately 200 proteins exhibited higher PSOH levels in 10-week-old $Cse^{-/-}$ brains than in 18-month-old WT littermates, suggesting that CSE deficiency results in elevated steady-state oxidative

damage (Supplementary Table 4), despite increased levels of some antioxidant enzymes (Extended Data Fig. 2).

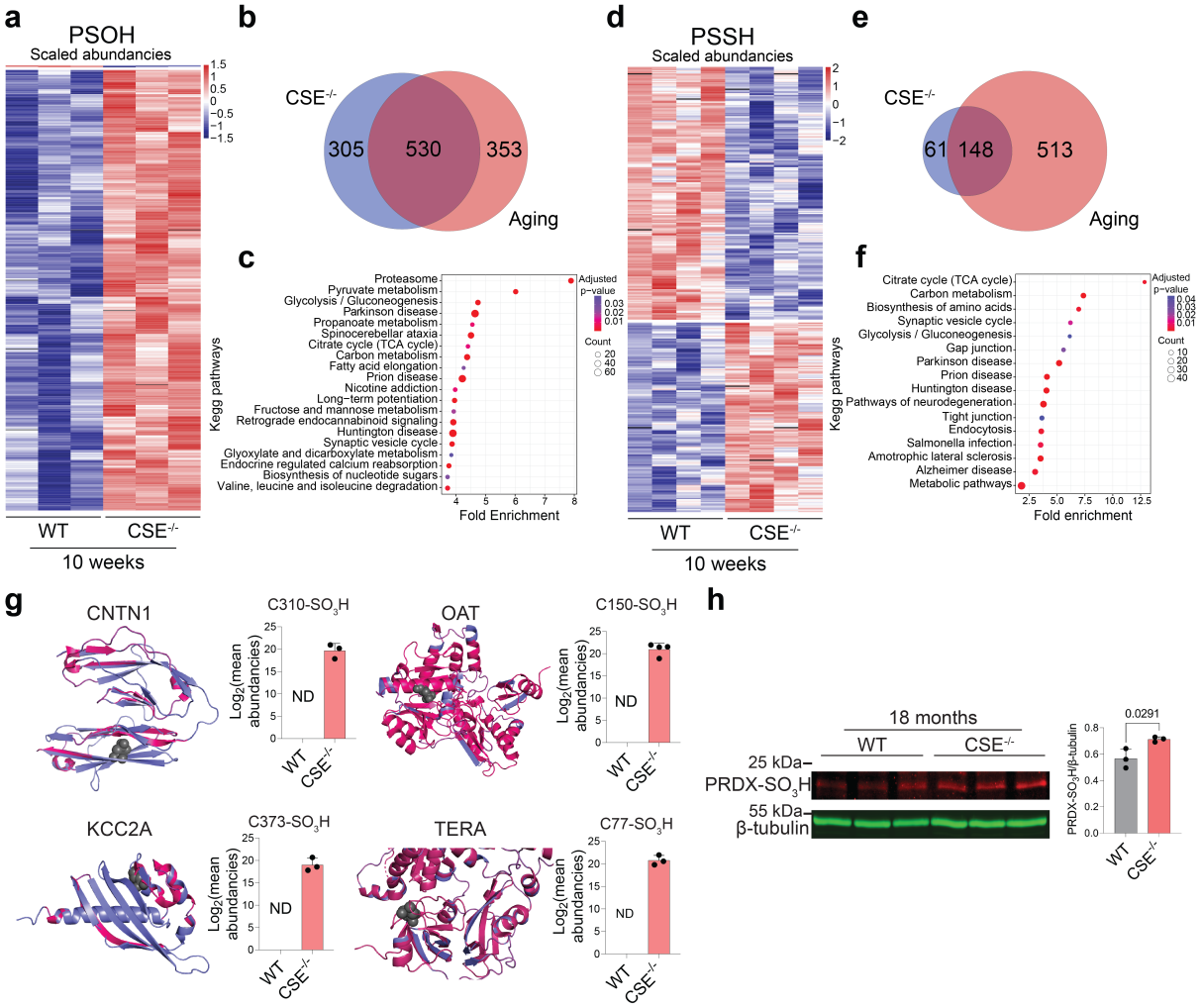


Figure 2. *Cse*$^{-/-}$ mice exhibit higher PSOH and PSO$_3$H levels but lower PSSH, shorter lifespan and spontaneous formation of neurofibrillary tangles. (**a**) Heatmaps of the significant PSOH changes found in the *Cse*$^{-/-}$ 10-week-old mice compared to the wild type (WT) 10-week-old mice (n = 3; FDR adjusted p value ≤ 0.05). The control 10-week-old mice are the same as in Fig.1. (**b**) Venn diagram comparison of sulfenylated targets found to be significantly affected by age and *Cse* knockout. (**c**) KEGG pathway enrichment analysis of proteins showing significant PSOH changes in *Cse*$^{-/-}$. (Benjamini adjusted p-value ≤ 0.05; color gradient indicates adjusted p-values and circle size the number of proteins). (**d**) Heatmaps of the significant PSSH changes found in the *Cse*$^{-/-}$ 10-week-old mice compared to the wild type (WT) 10-week-old mice (n = 4; FDR adjusted p value ≤ 0.05). (**e**) Venn diagram comparison of persulfidated targets found to be significantly affected by age and *Cse* knockout. (**f**) KEGG pathway enrichment analysis of proteins showing significant PSSH changes in *Cse*$^{-/-}$. (Benjamini adjusted p-value ≤ 0.05; color gradient indicates adjusted p-values and circle size the number of proteins). (**g**) Prediction of the structural changes caused by cysteine sulfonylation found exclusively in *Cse*$^{-/-}$ mice. Modeling was performed using VIENNA-PTM. The original crystal structure is depicted in pink, and the predicted model in blue. Contactin-1 (CNTN1; 3S97.pdb);[34] Ornithine aminotransferase (OAT; 2OAT.pdb);[35] Calcium/calmodulin-dependent protein kinase type II subunit alpha (KCC2A; 1HKX.pdb);[36] Transitional endoplasmic reticulum ATPase (TERA; 1R7R.pdb).[37] (**h**) PRDX sulfonylaiton levels in 18-

month-old WT and *Cse*$^{-/-}$ mice. The intensities were normalized to the β-tubulin expression levels. Values represent mean ± SD (Student's t-test n = 3).

A substantial overlap was observed between proteins with elevated PSOH levels in *Cse*$^{-/-}$ mice and those with increased PSOH levels in aging WT littermates (Fig. 2b). Pathways critical for healthy neuronal function were particularly enriched among these proteins (Fig. 2c, Extended Data Fig. 4c).

Conversely, a marked reduction in PSSH levels was observed in *Cse*$^{-/-}$ mice (Fig. 2d, Extended Data Fig. 4d,e). Approximately 70% of proteins showing decreased PSSH in *Cse*$^{-/-}$ mice exhibited similar declines in aging mice (Fig. 2e). Pathway enrichment analyses revealed patterns consistent with those observed in aging (Fig. 2f, Extended Data Fig. 4f). These findings underscore the pivotal role of CSE in regulating the PSOH to PSSH switch in the aging brain, highlighting its importance in maintaining redox homeostasis and neuronal health.

Age-induced PSSH to PSO_3H transition is more profound in Cse$^{-/-}$ mice

Consistent with the reaction scheme depicted in Fig. 1a, both aging and *Cse*$^{-/-}$ mice are expected to exhibit increased thiol oxidation, specifically sulfonylation (PSO_3H). While established methods for selectively labeling and enriching PSO_3H are lacking, we analyzed proteome data obtained by lysing tissues with NBF-Cl, which blocks all thiols, including sulfenic acids (Fig. 1b), thereby preventing unwanted cysteine oxidation during sample preparation. Out of 645 detected sulfonylated peptides (632 cysteine sites), 382 (388 cysteine sites) were absent in all 10-week-old WT mice, indicating that both aging and CSE deficiency are associated with increased PSO_3H levels (Supplementary Table 5). Using the criterion that peptides must be present in at least three out of four measured samples, we quantified changes in over 200 peptides (Extended Data Fig. 4g, Supplementary Table 5). Among these, 179 cysteine sites were common to all samples, 27 were uniquely identified in 18-month-old mice, and 30 in *Cse*$^{-/-}$ mice (Supplementary Table 5). It is worth mentioning that these observations are limited by the stochastic nature of data-dependent analysis.

To assess the structural impact of sulfonylation, we selected proteins with known crystal structures that showed significant increases in sulfonylation in aging and/or *Cse*$^{-/-}$ mice. Using Vienna PTM 2.0, a resource for exploring PTMs based on

molecular dynamics simulations,[38] we predicted the effects of PSO_3H on these protein structures. Overlaying the original crystal structures with those modeled for PSO_3H revealed conformational changes in all analyzed proteins (Fig. 2g, Extended Data Fig, 4i-n). In the modeled proteins, sulfonylated cysteines were predominantly located in beta-sheet domains or loops preceding beta-strands. Immunoblotting for the well-defined sulfonylated proteins PRDX[39] (Fig. 2h) and DJ-1[40] (Extended Data Fig. 4h) further confirmed the critical role of endogenously produced H_2S in regulating PSO_3H levels.

Age-induced cysteine PTMs contribute to the LLPS of synapsin 1

To elucidate the mechanisms underlying these observations, we conducted a detailed analysis of the proteomic data, which revealed that two major classes of proteins are particularly susceptible to age-related thiol remodeling: (1) metabolic enzymes and (2) structural and signaling proteins involved in neuronal structure, synapse organization, vesicle-mediated transport, and neurotransmission regulation. Traditional models of PTM-mediated signaling propose that modifications result in either a gain or loss of protein function. We selected lactate dehydrogenase (LDHB), pyruvate kinase (PKM) and pyruvate carboxylase, all proteins exhibiting age-dependent changes in PSOH and PSSH levels, and assessed their enzymatic activities in brain lysates. Surprisingly, no significant changes in enzyme activity were observed across different ages or in *Cse*$^{-/-}$ mice, even after exogenous H_2S supplementation (Extended Data Fig. 5). However, we noted that >30 % of proteins whose thiol redox status changes with aging overlaps with proteins reported to undergo LLPS[41] (Fig. 3a).

This prompted us to hypothesize that age-induced thiol oxidation remodeling may influence the mesoscale organization of proteins in neurons, thereby regulating their function. Notably, synapsin 1, the most abundant phosphoprotein in nerve terminals and a known phase-separating protein,[42] exhibited an age-dependent increase in PSOH and a decrease in PSSH (Fig. 3b). These changes were as pronounced in 10-week-old *Cse*$^{-/-}$ mice as in 18-month-old WT littermates (Fig. 3b). Similar age-related effects were observed for other synapsin isoforms (Extended Data Fig. 6a,b).

Synapsin 1 contains 3 cysteine residues (Fig. 3c), and we found that cysteine 360 (C360) existed in all three oxidation states, PSOH, PSSH and PSO_3H, with the

latter detected only in aged *Cse*$^{-/-}$ mice (Fig. 3d, Extended Data Fig. 6c). We estimated that ~3% of cysteine residues is sulfenylated in aged Cse$^{-/-}$ mice. C360 is located within the highly structured ATP-binding domain of synapsin 1, which is responsible for its multimerization (Fig. 3c). While PTMs in this region are not expected to directly affect phase separation, a process primarily governed by the intrinsically disordered regions of synapsin 1,[42,43,44] we designed a protocol to prepare different redox forms of synapsin 1 (Extended Data Fig. 6d) and compared their phase separation behavior. We used H_2O_2 treatment of fully reduced synapsin 1 as a method to generate PSOH (and/or PSSP) mimicking the intracellular thiol oxidation.[45,46] As shown in numerous previous studies, co-treatment with H_2O_2 and H_2S was used to transiently generate PSSH,[47–50] also mimicking intracellular mechanism for PSSH generation. PSO_3H was generated by adding H_2O_2 to protein containing small amounts of DTT. The role of DTT was to prevent disulfide formation and drive cysteine hyperoxidation. It is worth noting that this strategy also leads to the formation of PSO_2H, so we refer to it as PSO_xH (x = 2,3) (Extended Data Fig. 6d). Addition of H_2S to fully reduced protein was used as a negative control for PSSH, whereas treatment of iodoacetamide (IAM)-blocked protein thiols with H_2O_2 served as a control for methionine oxidation. Our experimental design deliberately aimed to mimic the continual formation and interconversion of these oxidative and persulfidated states, analogous to the dynamic conditions in cells where fluxes of H_2O_2 and/or H_2S continuously reshape the redox landscape (Supplementary Text).

When incubated with a crowding agent (3 % PEG 3,000), all redox forms of synapsin 1 readily formed condensates (Fig. 3e). However, synapsin 1 PSO_xH formed significantly larger droplets than the fully reduced protein, while PSSH resulted in smaller droplets (Fig. 3e,f, Extended Data Fig. 6e). These condensates exhibited dynamic behavior and recovered promptly after photobleaching, but with distinct recovery kinetics (Fig. 3g, Extended Data Fig. 6f). The recovery rate and percentage increased for synapsin 1 PSO_xH (11.6 s *vs.* 14.5 s, 15 % increase in recovery) but decreased for PSSH (29.9 s *vs.* 14.5 s; 35 % decrease in recovery) (Fig. 3g, Extended Data Fig. 6g). From the $t_{1/2}$, we estimated the apparent diffusion coefficient (*D*app) of the protein molecules to be 6.2, 7.7 and 3.0 x 10^{-4} μm^2 s^{-1} for the PSH, PSO_3H and PSSH, respectively.

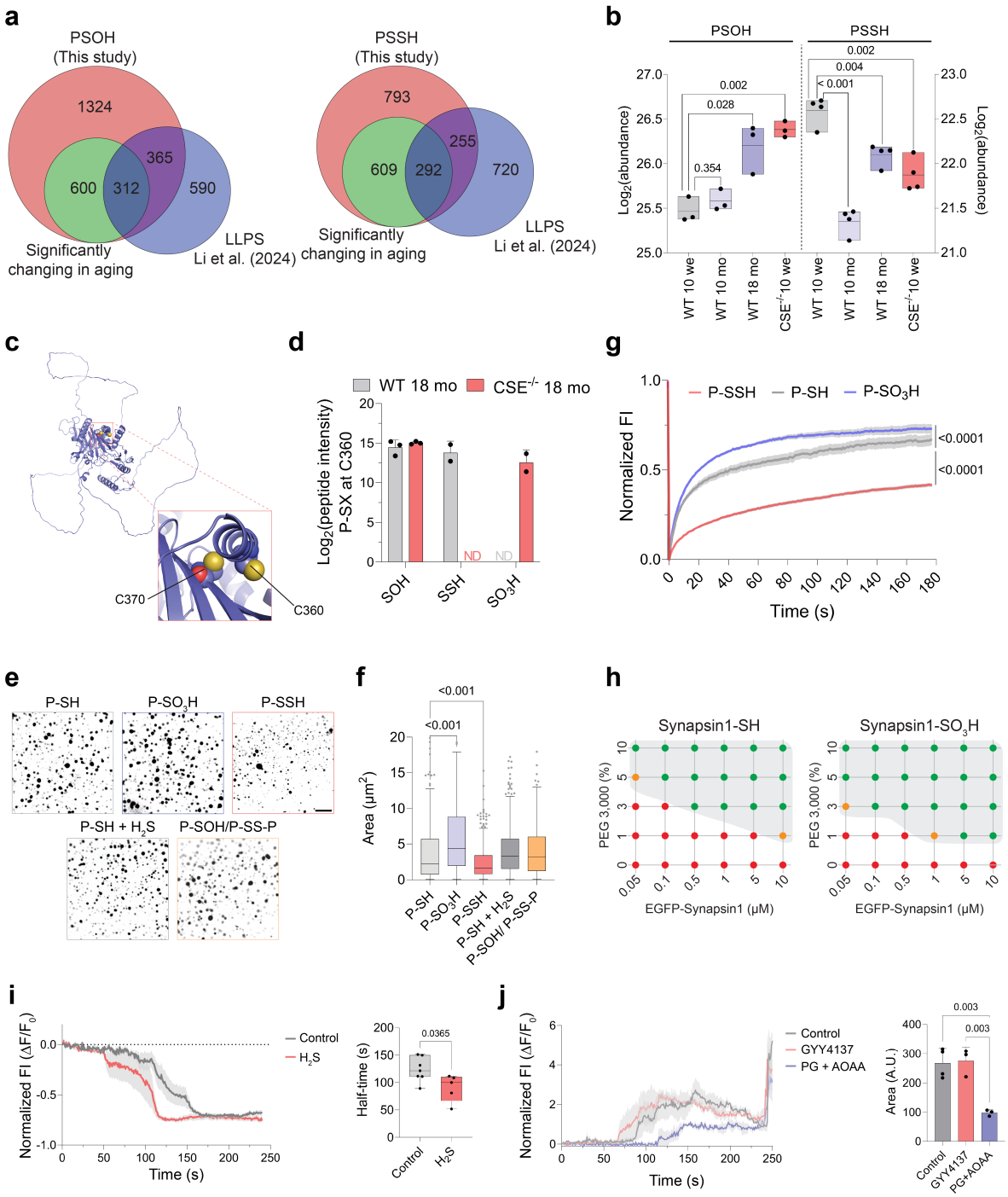


Figure 3. Age-related thiol remodeling of synapsin 1 controls its liquid-liquid phase separation and neurotransmitter release. (**a**) Venn diagram representing the overlap of (left) sulfenylated or (right) persulfidated proteins identified in our study (all proteins are red circle, significantly changing with aging are green) with proteins found to undergo biomolecular condensation in Li et al, 2024.[51] (**b**) Boxplot of the age-induced sulfenylation (PSOH) and persulfidation (PSSH) of synapsin 1 (PSOH: n = 3, PSSH: n = 4, Welch's t-test from proteomic analysis). (**c**) Structure of synapsin 1 highlighting two of its cysteines C360 and C370. (**d**) Changes of sulfenylation (SOH), persulfidation (SSH), and sulfonylation (SO_3H) of the cysteine 360 but not C370, could be observed in WT and *Cse*$^{-/-}$ 18 months old mice (n = 3, ND: Non-Determined). (**e**) Representative microscopy images for EGFP-synapsin 1 condensates (10 µM in the presence of 3% PEG3000) formed under different cysteine modifications. Scale bar = 20 µm. (**f**) The box and whiskers plots (Tukey style, outlier in gray dots) represent the distribution of the droplet area in µm^2 among the different cysteine

modifications (n ≥ 2 independent preparations, N = 360-840 data points per condition, one-way ANOVA). (**g**) Fluorescence recovery after photobleaching quantification of EGFP-synapsin 1. Means are shown as line and standard error as a shade of grey (n ≥ 2 independent preparations, N = 30-50 condensates per condition, two-way ANOVA, Sidak posthoc test). (**h**) Summary of the phase separation behavior of the reduced and sulfonylated EGFP-synapsin 1 with increased concentration of PEG-3000. (**i**) Kinetics of mScarlet-synapsin 1 droplet dissolution in the synapse of primary neurons, treated or not with 100 µM Na_2S, upon stimulation with 92.5 mM KCl (n = 3 animals, a few preparations per animal, Student's t-test). (**j**) The neurotransmitter release from mouse primary neurons without or pre-treated with 100 µM GYY4137 or 1 mM mixture of propargylglycine (PG) and aminooxyacetic acid (AOAA) for 1 h. Synaptic vesicle release was triggered by perfusion of neurons with 92.5 mM KCl; the fluorescence of synaptophysin-pHluorin was used as a readout. Means are shown as lines and standard error of the mean as a shade of grey. The area under the curve was calculated for each measurement (n ≥ 3 animals, a few preparations per animal, one-way ANOVA, Tukey's HSD Test for multiple comparisons).

Droplets formed by synapsin 1 treated with H_2O_2 (to generate a PSOH/disulfide mix) or H_2S (expected to be non-reactive) were indistinguishable in size and FRAP recovery kinetics from those formed by fully reduced synapsin 1 (Fig. 3e,f, Extended Data Fig. 6f). The lack of effect from H_2O_2 treatment alone also excluded the possibility that methionine oxidation influences LLPS, as suggested for ataxin.[52] This is further confirmed by the absence of FRAP recovery differences between IAM-blocked synapsin treated or not with H_2O_2 (Supplementary Fig. 4). Observations of droplet wetting revealed clear differences in liquid properties: PSO_xH promoted faster and more extensive wetting compared to PSH, while persulfidated synapsin 1 exhibited minimal wetting, with droplets remaining small (Extended Data Fig. 6h). These findings demonstrate that the cysteine redox status of synapsin 1 modulates its phase separation propensity, with sulfonylation enhancing LLPS. Indeed, the phase diagram of synapsin 1 LLPS confirmed that sulfonylated proteins phase separate at lower concentrations of crowding agent and protein (Fig. 3h, Extended Data Fig. 6i,j). Synapsin 1 is present at approximately 100 µM in nerve terminals.[42] Given the phase-diagram shift we observed for PSO_3H, sulfenylation of only about 3% of the protein population would be sufficient to drive the onset of phase separation.

The smaller condensates, slower diffusion, and wetting observed for persulfidated synapsin 1 suggest that PSSH restricts its phase separation capability. This implies that H_2S-induced PSSH formation could significantly impact synaptic vesicle dispersion and neurotransmitter release. Consistent with this, exposure of primary neurons to H_2S accelerated KCl-induced dispersion of synapsin 1 from presynaptic terminal in primary hippocampal neurons (Fig. 3i). Similarly, treatment of

primary mouse neurons with the slow releasing H_2S donor GYY4137 enhanced synapsin 1 dispersion and neurotransmitter release, whereas CSE inhibition delayed the release by approximately twofold and reduced overall synaptic vesicle release (Fig. 3j, Supplementary movies 1-3). These results provide a mechanistic explanation for the previously proposed role of endogenous H_2S in neurotransmitter release,[53–55] particularly in the context of neurodegenerative diseases associated with reduced CSE expression levels and impaired neurotransmitter release.[3,8–10]

C73 in G3BP2 is a regulator of stress granule formation

In addition to the molecular crowding-induced phase separation seen in synapsin 1, proteins also undergo condensate formation when interacting with RNAs.[56–61] One subset of such ribonucleoprotein granules is stress granules (SG), which are initiated by various stressors to arrest translation initiation and protection of RNAs.[62,63] Prompted by the observations that the thiol oxidation status of synapsin 1 affects its ability to phase separate, we overlapped the datasets obtained for aging PSSH and PSOH with proteomes of SGs and found that ~1/3 of all proteins reported to be associated with SGs show significantly lower PSSH levels and significantly higher PSOH levels (Extended Data Fig. 7a,b). Among them, we identified several well-defined SG proteins (Extended Data Fig. 7c,d,e), but we focused our analysis on G3BP2 (Ras GTPase-activating protein-binding protein 2), a key initiator of SG formation.[58,59] G3BP2 displayed an increase in PSOH and a similar decrease in PSSH levels, caused by aging or absence of CSE (Fig. 4a).

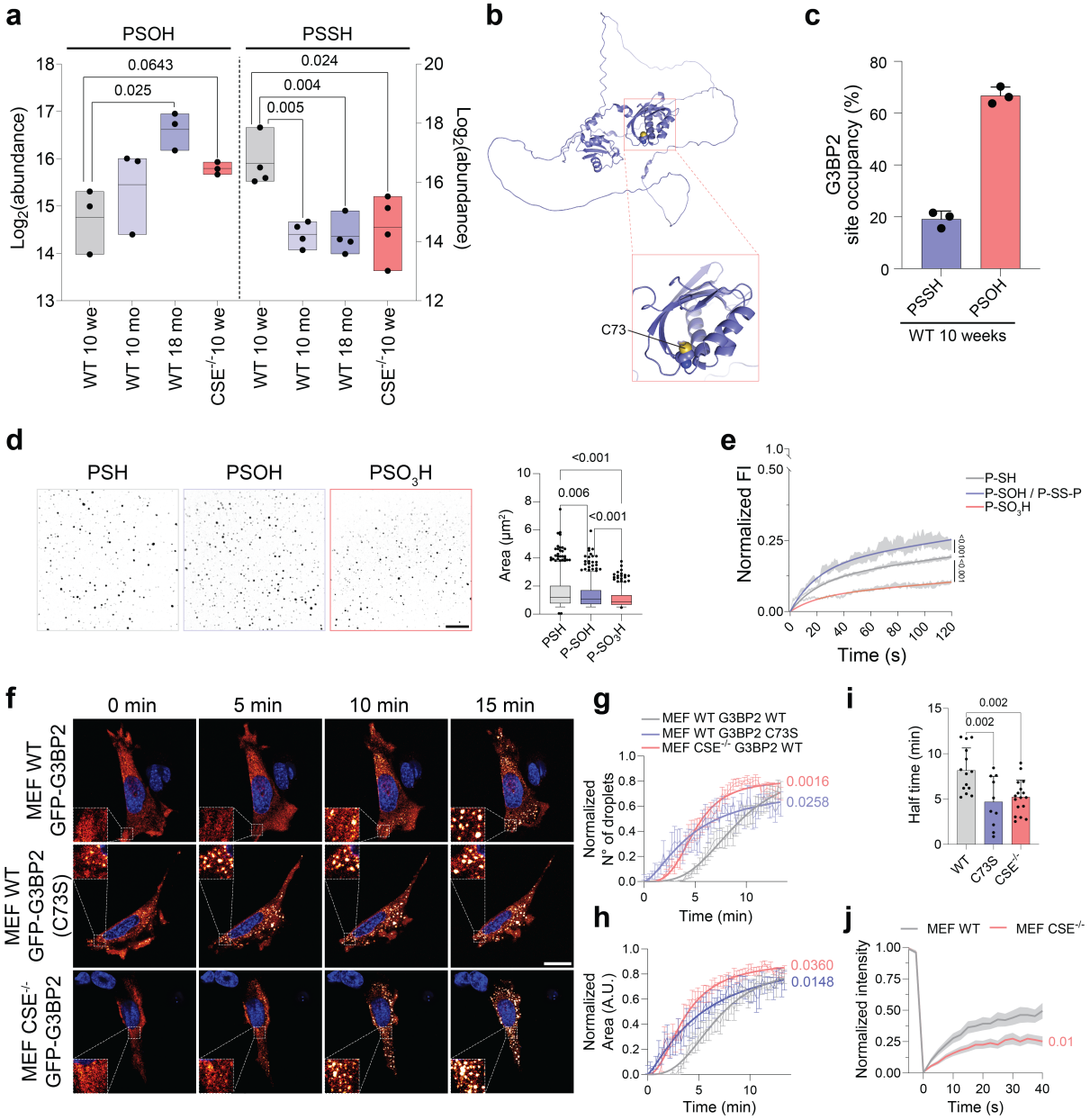


Figure 4. Thiol modifications of G3BP2 affect its biomolecular condensation. (**a**) Boxplot of the age-induced sulfenylation (PSOH) and persulfidation (PSSH) of G3BP2 (PSOH: n = 3, PSSH: n = 4, Welch's t-test from proteomic analysis). (**b**) G3BP2 Alphafold predicted structure (AF-P97379-F1-model_v4.pdb). Cysteine 73 is unique and present in the NTF2-like domain of the protein. (**c**) G3BP2 site occupancy of PSSH and PSOH in 10-week-old WT brain samples. Site occupancy was obtained using the protocol depicted in Extended data Fig 7h. (**d**) Phase separation of G3BP2 with different cysteine PTMs. Prior to phase separation induction, G3BP2 (10 µM) underwent treatment with DTT (100 µM; PSH), H_2O_2 (200 µM; PSOH), or a combination of DTT and H_2O_2 (100 µM and 200 µM respectively, PSO_xH), for 30 min at 37 °C. LLPS was induced using 50 ng/µl of total RNA extract, and images were taken 5 min after induction. Quantification of droplet area of n ≥ 3 independent preparation, one-way ANOVA, Tukey's HSD Test for multiple comparisons (N≥ 400 droplets), Scale bar = 20 µm. (**e**) Kinetics of FRAP recovery of G3BP2-Cy3 condensates formed with reduced (PSH), sulfenylated (PSOH) and sulfonylated (PSO_xH) G3BP2. Colored lines represent the mean of all kinetic fits, and 95% CI errors are represented as shades of grey. n ≥ 3 independent preparation, N≥56 droplets. (**f**) Arsenite stress (500 µM) induced SG formation in WT mouse embryonic fibroblasts (MEF) expressing either the wild type (WT) or the C73S mutant of GFP-

G3BP2 or in *Cse*$^{-/-}$ MEFs expressing the WT GFP-G3BP2 (representative confocal images of the real-time recording, n ≥ 10 cells from n ≥ 4 biological experiments). Scale bar = 20 µm. (**g-h**) Quantification of the (**g**) number and (**h**) size of G3BP2 SG upon arsenite treatment. Mean and non-fits are represented by continuous line and bars represent standard error (N ≥ 10 cells from n ≥ 4 biological replicates, two-way Anova; p-value indicates comparison to the MEF WT expressing G3BP2 WT [control]). (**i**) Half-time of G3BP2 SG formation calculated from the nonlinear regression. Dots represent quantification from individual cells, N ≥ 10 cells, n ≥ 5 biological experiments. One-way ANOVA, Tukey's HSD Test for multiple comparisons). (**j**) In-*cellulo* FRAP kinetics of GFP-G3BP2 in WT or *Cse*$^{-/-}$ MEFs. Standard error is represented as shades of gray (N = 10 cells from n ≥ 5 biological experiments, with average of 1-2 droplets per cells two-way ANOVA, Sidak posthoc test).

G3BP2, the predominant paralogue expressed in brain,[64] contains a single cysteine residue (C73) located within the structured beta-sheet domain (Fig. 4b), which appeared early in evolution (Extended Data Fig. 7f,g). We also designed an experiment to estimate the steady-state occupancy of C73 by PSSH and PSOH, showing that in the frontotemporal regions of the brain of 10-week-old mice, C73 exists ~65% in the form of PSOH and ~20% as PSSH (Fig. 4c, Extended Data Fig. 7h), suggesting an important role of these modifications on G3BP2 function.

Using AlphaFold generated structures and Cyspka,[65] we estimated the pK_a of C73 and obtained a value <0 (Supplementary Fig. 5a, pK_a = -2.1287). Interestingly, C360 in synapsin 1 showed an equally strong local effect on pK_a (Supplementary Fig. 5b, estimated pK_a = -6.0564). This indicates a highly acidic cysteine that exists predominantly as a strongly stabilized thiolate under physiological pH, rendering it a reactive “hot spot”.

To address the potential effects of cysteine oxidation on G3BP2 phase separation, we first tested PSOH and PSO$_x$H forms of the recombinant protein (Extended Data Fig. 8a). Upon addition of RNA, droplet formation was observed in both cases, with G3BP2 PSO$_x$H forming significantly smaller condensates (Fig. 4d) that showed slower FRAP recovery and lower % recovery ($t_{1/2}$ = 55.0 s *vs.* 44.5 s, 42 % decrease; Fig. 4e, Extended Data Fig. 8b). In contrast, granules formed by G3BP2 PSOH showed faster kinetics and % of FRAP recovery ($t_{1/2}$ = 37.6 s *vs.* 44.5 s, 25 % increase; Fig. 4e, Extended Data Fig. 8b), suggesting that sulfenylation enhances the diffusion rate of G3BP2. This effect was not observed in IAM-blocked G3BP2, confirming that it is caused by cysteine modifications rather than methionine oxidation (Extended Data Fig. 8c,d).

Because no proper amino acid mimetic exists for PSOH (PSOH is expected to be deprotonated at physiological pH due to its pK_a ~7), [45] the closest approximation is a cysteine-to-serine mutation. To test whether PSOH influences SG formation *in vivo*, we expressed GFP-tagged wild type or C73S mutant G3BP2 in mouse embryonic fibroblasts (MEF) and monitored their response to arsenite-induced stress. [11] All cells expressing C73S G3BP2 exhibited small pre-formed SGs even in the absence of stress (Fig. 4f, Supplementary movie 4), which continued growing in size and number significantly faster than WT granules upon arsenite exposure, although the normalized number and size of droplets per cells after 15 min of arsenite stress were comparable between the two conditions (Fig. 4g,h,i, Supplementary movie 4). These data suggest that the total pool of G3BP2 was unaffected, but rather that its biomolecular condensation kinetics were altered.

A similar kinetic profile and behavior was observed in *Cse*$^{-/-}$ MEF cells Fig. 4f-i, Supplementary movie 4), in which BTD trapping followed by immunopulldown and MS analysis revealed that untreated *Cse*$^{-/-}$ MEF contain levels of PSOH compared to those of WT cells treated with arsenite (Extended Data Fig. 8e,f). FRAP recovery of G3BP2 SG in *Cse* $^{-/-}$ MEFs was significantly slower than in WT cells (Fig. 4k, Extended Data Fig. 8g, Supplementary movie 5). This may be explained by higher levels of protein cysteine hyperoxidation in these cells, as reported previously,[50] which aligns with the *in vitro* observations for PSO_xH G3BP2 condensates (Fig. 4e).[12]

G3BP2 persulfidation leads to dissolution of stress granules

Our previous work identified intertwined connection between PSOH and PSSH, in which a signaling wave of PSOH was followed by a resolving wave of PSSH.[50] To understand the role of PSSH in G3BP2 SG dynamics, we examined changes in PSOH and PSSH in cells exposed to arsenite, as well as during the recovery from stress. The sulfenylation profile showed that arsenite treatment causes a global increase in cellular PSOH, which subsequently declines during the recovery phase. PSSH, however, was significantly reduced during the stress but increased markedly during recovery (Fig. 5a, Extended data Fig 9a). BTD or dimedone switch labeling followed by immunopulldown of G3BP2 allowed us to assess the kinetics of its sulfenylation and persulfidation, respectively, and these changes mirrored the global cellular trend (Fig. 5b, Extended data Fig. 9b). Proteomic analysis identified that 10-15% of G3BP2's cysteine is present in the persulfidated form (Extended data Fig. 9c, Supplementary

Fig. 6). These observations suggested that C73 may function as a redox switch, converting from droplet-stimulating PSOH to droplet-destabilizing PSSH.

To test this hypothesis, we first turned to purified protein. As G3BP2 contains only one cysteine, the most efficient way to generate the persulfide is to first produce the G3BP2 -TNB adduct using Ellman's reagent and then form PSSH by adding near-equimolar H_2S (Extended data Fig. 8a).[66,67] Pre-formed droplets of G3BP2-TNB (indistinguishable in size from control G3BP2, Extended data Fig. 9d) began dissolving upon H_2S addition and fully disappeared as the reaction progressed, indicating that persulfidation indeed dissolves G3BP2 condensates (Fig. 5c, Supplementary movie 6). This effect was not observed when H_2S was added to fully reduced protein (Extended data Fig. 9e).

Next, we monitored H_2S-induced dissolution of G3BP2 granules *in cellulo*. MEF cells expressing either WT or C73S GFP-tagged G3BP2 were exposed to 500 μM arsenite stress followed by H_2S addition. Upon H_2S treatment, immediate dissolution of SGs could be recorded in real time (Fig. 5d, Supplementary movie 7). Because of the continued presence of a stressor, the rapid consumption of H_2S by cells[68] and its loss to the gas phase[69], SGs reformed over time; however, complete dissolution could be re-induced by a second bolus of H_2S (Fig. 5d, Supplementary movie 7). No SG dissolution was observed in cells expressing C73S G3BP2 mutant, confirming that this is cysteine redox-mediated process (Fig. 5d, Supplementary movie 8). The reversible nature of this process, together with dynamic PSOH/PSSH changes observed during the stress and recovery (Fig. 5b), suggests that endogenously produced H_2S plays an important role in regulating SG formation and duration.

As we demonstrated, PSSH levels of G3BP2 decline in the aging brain, and even more markedly in *Cse* knockout animals, potentially impairing the ability of cells to dissolve SGs. Addition of CSE inhibitors during the recovery phase, when stressor had been removed, slowed recovery and maintained high SG levels, supporting the essential role of CSE-dependent persulfidation in SG disassembly (Extended data Fig. 9f,g). Indeed, whereas SG dissolved in WT cells one hour after stress removal, their number and size remained unchanged in *Cse*$^{-/-}$ MEFs (Fig. 5e-g).

We further tested this hypothesis in a more brain-relevant cell type, striatal neurons (STHdh). STHdh cells derived from Huntington's disease mice (STHdh$^{Q111/Q111}$) have

barely detectable CSE and PSSH levels relative to WT-derived STHdh$^{Q7/Q7}$ cells.[4] Arsenite stress caused a time-dependent increase in SG number and size in STHdh$^{Q7/Q7}$ cells, with recovery reducing this number (Extended Data Fig 10a,b). Addition of H_2S donor GYY4137 during recovery almost completely dissolved the remaining SG. In contrast, STHdh$^{Q111/Q111}$ cells displayed stronger and faster responses to arsenite stress, and even after 1 h of recovery, still contained significant number of SGs (Extended Data Fig 10a,b), akin to Cse$^{-/-}$ MEFs. While GYY4137 reduced SG numbers in these cells, this effect was modest, consistent with limited benefit of H_2S donors in cells that are generally unable to convert PSOH to PSSH and instead accumulate higher PSO$_x$H levels (Fig. 1a).[50]

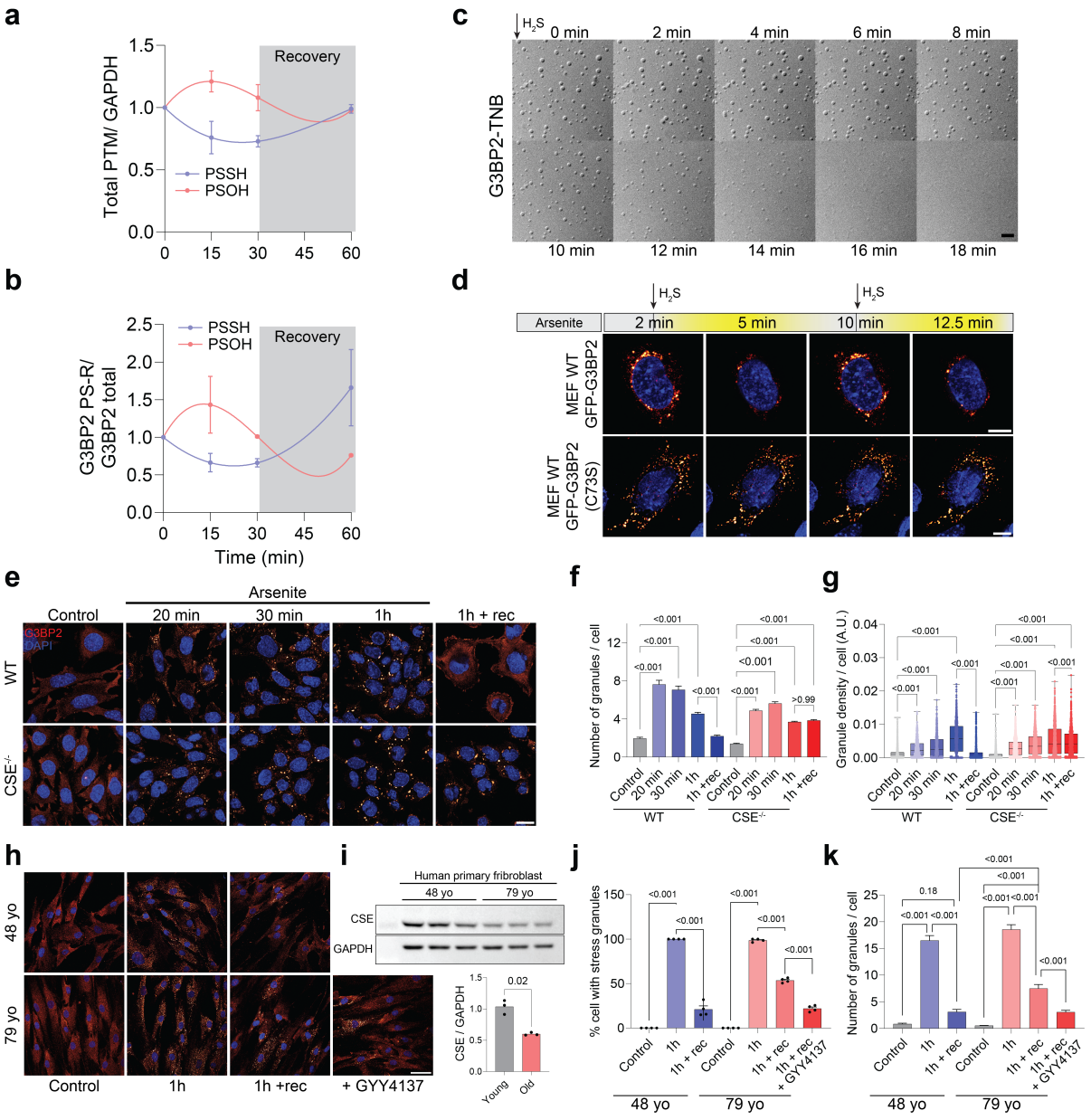


Figure 5. Persulfidation of G3BP2 leads to SG disassembly. (**a**) Global and (**b**) G3BP2 PSOH and PSSH changes in MEF cells treated with 500 µM $NaAsO_2$ for 15 and 30 min. After 30 min $NaAsO_2$ was removed, and cells were allowed to recover for 30 min (recovery). BTD-labelling was used for PSOH, and the dimedone-switch method with DCP-Bio1 was used for PSSH (n = 2, ± SD). (**c**) Real time dissolution of G3BP2 condensates initiated by protein persulfidation. 20 µM of G3BP2 were incubated with 40 µM of DTNB and 50 ng/µl of RNA for 10 min prior addition of 50 µM of H_2S and recording (Representative DIC images of the dissolution of 3 separate reconstitutions). Related to the Supplementary movie 6. Scale bar = 10 µm (**d**) Representative images of confocal live cell monitoring of G3BP2-GFP condensate dissolution upon addition of H_2S in WT MEF expressing GFP-G3BP2 WT or GFP-G3BP2 (C73S). Na_2S (100 µM) was added 15 min after SG formation was initiated with arsenite (500 µM). n = 3 biological replicates. Related to the Supplementary movie 7. Scale bar = 10 µm. (**e**) Representative images and quantification of the (**f**) number and (**g**) density of G3BP2 condensates formation in WT and *Cse*$^{-/-}$ MEF upon 500 µM arsenite. Scale bar = 20 µm. Recovery was conducted for 1 h. Quantification was performed per cell (n = 3 biological replicates, N > 550 cells quantified, one-way ANOVA, Tukey's HSD Test for multiple comparisons). (**h**) Representative images of human primary fibroblast from a 48- and 79-year-old subject exposed to 500 µM arsenite over time. Recovery was conducted for 1 h, 200 µM of GYY4137 was used on the 79-year-old cell line (n = 3 independent replicates, several images per replicate). (**i**) Western blot of CSE levels in the human fibroblast showing decreased CSE levels (normalized to GAPDH). (n = 3, Welch´s t-test). (**j-k**) Quantification of (**j**) number and (**k**) density of the G3BP2 condensates in the human primary cell lines (n = 4, N > 300 cells quantified, one-way ANOVA, Tukey's HSD Test for multiple comparisons).

To confirm that these effects also occur in aging cells, we used human primary fibroblasts from a 48-year-old donor and 79-year-old donor (Fig. 5h). Fibroblasts from the older donor exhibited clearly reduced CSE expression (Fig. 5i), corroborating our observations that aging leads to CSE decline. When exposed to arsenite stress and subsequently allowed to recover, fibroblasts from the old donor showed markedly impaired SG dissolution compared to those from the young door, an effect that was rescued by GYY4137 (Fig. 5j,k).

These results confirm the importance of endogenous H_2S production in maintaining the normal SG kinetics and highlight the therapeutic potential of exogenous H_2S donors for dissolving pathological condensates. We recently described a mechanism by which ergothioneine (ET) acts as a pro-longevity drug with long-term healthspan benefits, serving as an alternative substrate for CSE, producing H_2S, and increasing protein persulfidation.[70] As a proof-of-concept, we compared the ability of MEF cells treated with ET to recover from the stress. ET treatment decreased SG size and number, but only in WT cells. *Cse*$^{-/-}$ cells, unable to metabolize ET to H_2S, were unaffected by the treatment (Extended Data Fig 10c,d).

Age-induced redox disbalance leads to protein aggregation

The inability of cells to dissolve biomolecular condensates is considered one of the key features of aging and a driver of pathological protein aggregation.[71–73] TDP-43, TAR DNA-binding protein 43, is a highly conserved nuclear RNA/DNA-binding protein involved in the regulation of RNA processing and is normally localized to the nucleus. Accumulation of TDP-43 aggregates in the cytosol of neurons is a common feature of many neurodegenerative diseases, including amyotrophic lateral sclerosis, frontotemporal dementia and Alzheimer's disease.[74–78] TDP-43 is a component of SGs, and its predominant cytoplasmic localization is often interpreted as a sign of pathogenicity.[74,78] We assessed TDP-43 levels in WT and *Cse*$^{-/-}$ cells and found them unchanged; however, the TDP-43 cytosol/nucleus ratio was significantly higher in *Cse*$^{-/-}$ cells and increased further under arsenite stress (Supplementary Fig. 7a,b). Colocalization studies of G3BP2 positive stress granules, with TDP-43, TIA-1 and EIF4G, showed marked differences between WT and *Cse*$^{-/-}$ cells exposed to stress (Supplementary Fig. 7c-e). *Cse*$^{-/-}$ cells exhibited larger G3BP2, TDP-43, and EIF4G positive granules (Supplementary Fig. 7d), although their number was not necessarily higher (Supplementary Fig. 7e), suggesting that impaired granule dissolution could create nucleation centers for protein aggregation. We therefore performed the filter trap experiments and confirmed that TDP-43 is indeed more aggregated in *Cse*$^{-/-}$ cells (Supplementary Fig. 8a).

In the light of our proteomics finding that aging is associated with cysteine (hyper)oxidation, whereas beneficial persulfidation is reduced, and that cysteine (hyper)oxidation drives biomolecular condensation, we hypothesized that aging, like *Cse* knockout, would result in stronger protein aggregation. Molecular dynamics modeling for some sulfonylated targets revealed that cysteine residues are typically located within or at the edges of beta-sheets, leading to significant conformational changes (Fig. 2g). If these changes mimic phosphorylation-driven effects (and hyperphosphorylation of certain proteins is linked to neurodegenerative disases), then proteins with hyperoxidized cysteine residues may be more prone to aggregation. To test this hypothesis, we treated WT and *Cse*$^{-/-}$ MEFs with H_2O_2 and performed a thermal proteome profiling stability assay, focusing on the beginning and end of the melting curve (47 ºC vs 57 ºC). The proteome of *Cse*$^{-/-}$ MEFs, which have reduced H_2S production to counteract thiol hyperoxidation,[4] was significantly destabilized by H_2O_2, with the majority of identified proteins losing their stability and aggregating from

the solution even at 47 ºC (Fig. 6a, Supplementary Table 6). These findings support the notion that the age-related shift from persulfidation to sulfonylation not only affects the LLPS propensity of proteins but also enhances their aggregation potential.

We therefore examined the levels of well-known neurodegenerative culprit, amyloid-β, in WT and *Cse*$^{-/-}$ brain samples using a filter trap assay and found significantly higher amyloid-beta aggregation in 18-month-old *Cse*$^{-/-}$ mice compared with WT (Fig. 6c). Aggregation of G3BP2 and TDP43 was not significantly affected, although both showed an upward trend in *Cse*$^{-/-}$ mice (Supplementary Fig. 8b,c). In contrast, TIA-1, a known SG component and prion-like protein, was significantly more abundant in aggregated fraction (Fig. 6d). Notably, levels of intramolecular disulfides were not different between WT and *Cse*$^{-/-}$ samples, emphasizing the importance of other redox cysteine PTMs (Supplementary Fig. 8d).

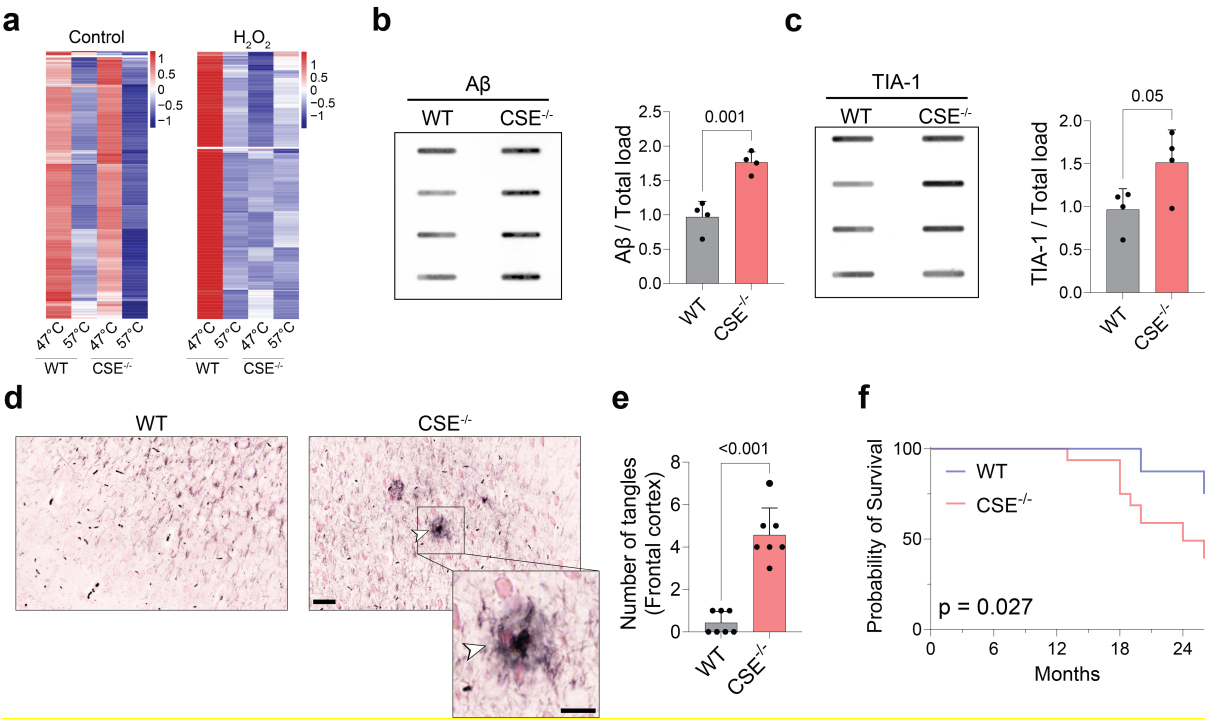


Figure 6. Age-induced thiol remodeling increases protein aggregability. (**a**) Thermal proteome stability assay between WT and *Cse*$^{-/-}$ MEF cells (n = 2). (**b-c**) Filter trap experiments on 18-month-old brain WT and *Cse*$^{-/-}$ mice lysate using antibodies against (**b**) Amyloid-β (Aβ) and (**c**) TIA-1. Intensities were normalized to the total load presented in Supplementary figure 11. (n = 4, Welch´s t-test, dots represent individual values and error bars indicates SD). (**d**) Gallyas silver staining of WT and *Cse*$^{-/-}$ 18-month-old mouse brain sections for the neurofibrillary tangles. Global stained sections are shown in Supplementary Fig. 9. The arrow points to the example of neurofibrillary tangle observed in the brain sections of *Cse*$^{-/-}$. Scale bar = 40 µm; zoomed image 20 µm. (**e**) Quantification of tangles observed in cortex is shown in the histogram. 7 images from 4 different animals were analyzed. (n = 4, Welsch´s t-test). (**f**) Survival rates of *Cse*$^{-/-}$ vs. WT mice. n = 16 per group (two individual lifespan experiments of

8 animals/group in each experiment). Kaplan-Meier survival analysis, Mantel-Cox long rank test.

To assess potential neurodegenerative pathology, we examined brain sections from 18-month-old *Cse*$^{-/-}$ mice and WT littermates for the presence of neurofibrillary tangles or tau aggregates though Gallyas silver staining. As expected, WT mice showed almost no tau pathology, with only one neurofibrillary tangle observed in the cortex of 3 out of 7 analyzed brain sections (Fig. 6e). By contrast, *Cse*$^{-/-}$ mice exhibited numerous neurofibrillary tangles throughout the brain, including the frontotemporal region, cerebellum, and hippocampus (Fig. 6e, Supplementary Fig. 9). Importantly, no tangles were observed in 2-month-old *Cse*$^{-/-}$ mice, indicating that their formation is age-dependent (Supplementary Fig. 10).

These findings suggest that aging, combined with reduced H_2S production, drives significant thiol remodeling, which may also have widespread implications for cellular survival in *Cse*$^{-/-}$ mice. These effects are unlikely to be restricted to the brain and may instead be widespread, as G3BP-dependent stress granule assembly and disassembly play a universal role in cellular stress protection. With aging, impaired resolution of biomolecular condensates can disrupt cellular homeostasis and contribute to a decline in healthspan, ultimately affecting overall lifespan. Indeed, *Cse*$^{-/-}$ mice exhibited higher mortality rate before reaching 18 months of age. Comparative lifespan analysis revealed that *Cse*$^{-/-}$ mice have a significantly shorter lifespan than their WT littermates (Fig. 6f).

Discussion

The origins of life are deeply intertwined with the presence of H_2S, which, alongside cyanide, played a pivotal role in the genesis of biomolecules.[79] Cysteine, in turn, catalyzed the first peptide syntheses,[80] while LLPS and biocondensate formation have been fundamental in shaping the evolution of life as we know it.[81–83] These fundamental chemical and biophysical processes remain essential for cellular function and homeostasis. This study reveals the transformative potential of cysteine PTMs on protein LLPS, highlighting the regulatory role of protein persulfidation while establishing a biochemical link between aging and phase separation.

The aging brain appears overwhelmed by oxidative stress, as evidenced by our sulfenylome and sulfonylome data. The role of reactive oxygen species (ROS) in aging has stirred both acclaim and controversy.[1,84,85] While ROS is critical during early developmental stages, potentially predisposing organisms to longer lifespans,[86,87] it becomes detrimental in aging organisms.[88] Our research demonstrates that steady state levels of PSOH, the first thiol oxidation step in the reaction with ROS, increase continuously with aging, eventually leading to PSO_3H. This process is partially mitigated by endogenous H_2S production. Notably, protein persulfidation promotes the dispersion of phase-separated condensates, whereas cysteine oxidation drives enhanced phase separation, ultimately leading to protein aggregation. In the aging brain, these changes could lead to (i) compromised synaptic release due to disrupted synapsin 1-synaptic vesicle condensates, (ii) increased and unresolved phase separation of G3BP2 and (iii) the accumulation and aggregation of proteins.

In both G3BP2 and synapsin 1, CysPka predicts exceptionally low apparent pKa values for their redox-active cysteines (≈ −2 for G3BP2 C73 and ≈ −6 for synapsin 1 C360) (Supplementary Fig. 5), indicating that these residues occupy highly thiolate-stabilized reactive hotspots. Notably, mutation of these cysteines to serine or glutamate produced opposite shifts in the hydrophobic character of their local environments: hydrophobicity decreased twofold around G3BP2 C73 but increased approximately twofold around synapsin 1 C360 (Supplementary Fig. 5). These divergent behaviours underscore that local packing effects are highly context-specific and that no single physicochemical parameter (e.g., hydrophobicity) uniformly explains the functional outcomes. Likewise, because PSSH, PSOH, and PSO_xH modifications are all expected to be deprotonated at physiological pH, changes in net charge cannot account for the markedly different effects of each oxidation state.

Instead, we propose that persulfidation at such thiolate hotspots acts as a general anti-sticker modification. By extending the cysteine side chain with an additional sulfur atom and increasing local solvation, polarizability, and conformational flexibility,[67] persulfidation disrupts thiolate-dependent contacts and introduces dynamic S–S exchange. These features collectively reduce the effective multivalency of the interaction network. In G3BP2, this could manifest as weakened coupling between the NTF2-like domain, low-complexity regions, and RNA, whereas in synapsin 1 it could diminish the cohesive interactions required for crowding-enhanced

condensation with synaptic vesicles. In both systems, the consequence is dissolution of the condensate.

By contrast, irreversible overoxidation to cysteine sulfonic acid introduces a rigid, strongly electronegative SO_xH group that acts as a local anchoring point, akin to phosphorylation,[89] thereby enhancing cohesion and promoting larger, more persistent droplets. Together, these observations indicate that the behaviour of cysteine redox PTMs is best understood through their differential effects on sticker strength rather than through global physicochemical variables such as net charge.

Neuronal transmission relies on the regulated secretion of neurotransmitters,[90] a process governed by synaptic vesicles whose dynamics are controlled by synapsin 1.[91] Given that impaired synaptic transmission is a hallmark of age-related neurodegenerative diseases, it is plausible that the age-induced thiol remodeling described in this study contributes to this process. Indeed, our recent studies demonstrate that *Cse*$^{-/-}$ mice exhibit impaired memory in novel object recognition, novel location, social novelty, and Barnes maze tests (Chakraborty et al. 2025, in press).

A hallmark of cellular homeostasis is the ability to assemble stress granules rapidly in response to stress to safeguard RNA, and to disassemble them efficiently once the stress is resolved.[71,92] With age, however, declining persulfidation and a concomitant increase in PSOH and PSO_xH species impair this resolution step: SGs persist even after the stressor is removed (Fig. 7). As oxidized proteins remain sequestered within condensates for prolonged periods, their altered interactions promote aberrant stabilization and eventually aggregation, establishing a self-reinforcing pathological loop. This defect is exemplified by *Cse*$^{-/-}$ cells, which fail to dissolve SGs long after stress withdrawal, a phenotype which can be rescued by supplying an H_2S donor. Thus, the age-associated loss of persulfidation predisposes proteins to prolonged LLPS and conformational states that favour aggregation, consistent with our observations of elevated protein aggregation and neurofibrillary tangle formation in *Cse*$^{-/-}$ mouse brain. These findings indicate that *Cse*$^{-/-}$ mice provide a valuable model for studying age-associated mechanisms of neurofibrillary tangle formation and Alzheimer's disease–like phenotypes, several of which are recapitulated at the cellular level. Notably, even short treatment of *Cse*$^{-/-}$ cells with

H_2O_2 results in a global leftward shift in their proteome melting curves, indicating increased protein aggregability.

It is worth noting that studied cysteine PTMs represent only a small portion of the known cysteine PTMs (Supplementary Text). All these modifications have an intertwined nature, meaning that age-induced changes in cysteine sulfenylation or persulfidation could impact other cysteine modifications, such as palmitoylation,[93] cyanylation,[94] itakonylation,[95] etc, all of which could have biological effects of their own.

Instead, we show that cysteine modifications exert diverse and highly specific effects on the biophysical behaviour of proteins, including their propensity for liquid–liquid phase separation. This thiol-based tuning of condensate dynamics likely represents an endogenous regulatory mechanism that extends beyond classical redox signalling, with the potential to influence broad cellular and metabolic processes. More broadly, these observations help explain why thiol signalling rarely conforms to a one-modification/one-target/one-function paradigm: the outcome of cysteine oxidation depends on how each modification alters the physical interaction landscape of the protein rather than on a singular biochemical switch. However, age-induced remodelling of these thiol modifications shifts the balance toward unresolved biomolecular condensation, ultimately leading to a global collapse of cellular homeostasis and predisposing proteins to pathological aggregation (Fig. 7).

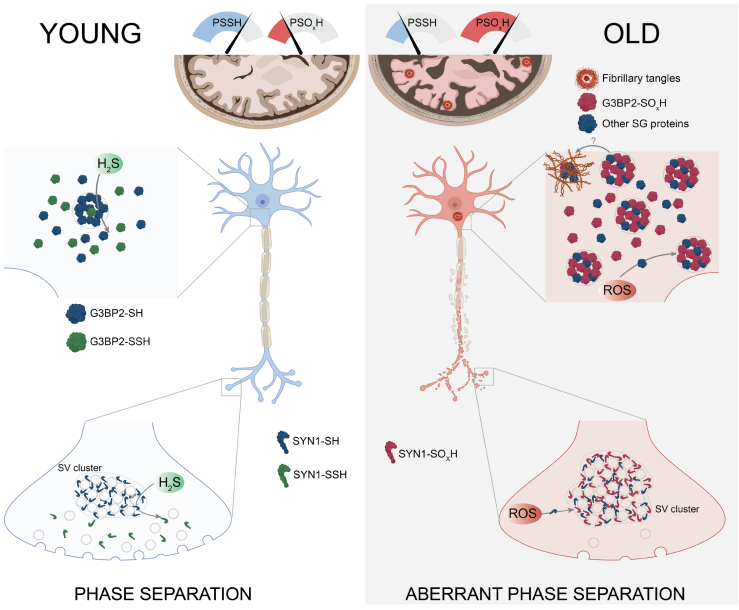


Figure 7. Age-dependent redox remodelling and its impact on the phase separation in the aging brain. In young cells, abundant PSSH maintains dynamic, reversible condensates

that enable efficient dissolution of stress granules and synaptic vesicle clusters. With aging, loss of PSSH and accumulation of PSO_xH shift these proteins toward more persistent condensates, promoting aberrant phase separation and predisposing cells to pathological aggregation.

The emergence of H_2S-releasing medicines offers a promising strategy for restoring the balance to age-related thiol oxidation and its effects on LLPS, providing potential therapeutic avenues for neurodegenerative disorders. A clear example is provided by ergothioneine, an alternative substrate of CSE that restores PSSH [11] and, as we demonstrate, promotes SG dissolution. Notably, ergothioneine intake has been linked to reduced cognitive decline in AD patients.[96] Persulfidation thus emerges as a unifying, reversible mechanism that counteracts LLPS at thiolate hotspots across diverse protein condensate systems.

References:

1. Gladyshev, V. N. Aging: progressive decline in fitness due to the rising deleteriome adjusted by genetic, environmental, and stochastic processes. *Aging Cell* 15, 594–602 (2016).
2. Paulsen, C. E. & Carroll, K. S. Cysteine-mediated redox signaling: Chemistry, biology, and tools for discovery. *Chem Rev* 113, 4633–4679 (2013).
3. Petrovic, D., Kouroussis, E., Vignane, T. & Filipovic, M. R. The Role of Protein Persulfidation in Brain Aging and Neurodegeneration. *Front Aging Neurosci* 13, 1–12 (2021).
4. Zivanovic, J. *et al.* Selective Persulfide Detection Reveals Evolutionarily Conserved Antiaging Effects of S-Sulfhydration. *Cell Metab* 30, 1152-1170.e13 (2019).
5. Bithi, N. *et al.* Dietary restriction transforms the mammalian protein persulfidome in a tissue-specific and cystathionine γ-lyase-dependent manner. *Nat Commun* 12, (2021).
6. Tyshkovskiy, A. *et al.* Identification and Application of Gene Expression Signatures Associated with Lifespan Extension. *Cell Metab* 30, 573-593.e8 (2019).
7. Tyshkovskiy, A. *et al.* Distinct longevity mechanisms across and within species and their association with aging. *Cell* 186, 2929-2949.e20 (2023).
8. Giovinazzo, D. *et al.* Hydrogen sulfide is neuroprotective in Alzheimer's disease by sulfhydrating GSK3β and inhibiting Tau hyperphosphorylation. *Proc Natl Acad Sci U S A* 118, e2017225118 (2021).
9. Paul, B. D. *et al.* Cystathionine γ-lyase deficiency mediates neurodegeneration in Huntington's disease. *Nature* 508, 96–100 (2014).
10. Snijder, P. M. M. *et al.* Overexpression of cystathionine γ-Lyase suppresses detrimental effects of spinocerebellar ataxia type 3. *Molecular Medicine* 21, 758–768 (2015).

11. Petrovic, D. *et al.* Ergothioneine improves healthspan of aged animals by enhancing cGPDH activity through CSE-dependent persulfidation. *Cell Metab* 37, 542-556.e14 (2025).
12. O'Flynn, B. G. & Mittag, T. The role of liquid–liquid phase separation in regulating enzyme activity. *Curr Opin Cell Biol* 69, 70–79 (2021).
13. Peeples, W. & Rosen, M. K. Mechanistic dissection of increased enzymatic rate in a phase-separated compartment. *Nat Chem Biol* 17, 693–702 (2021).
14. Xiao, H. *et al.* A Quantitative Tissue-Specific Landscape of Protein Redox Regulation during Aging. *Cell* 180, 968-983.e24 (2020).
15. Reisz, J. A., Bechtold, E., King, S. B., Poole, L. B. & Furdui, C. M. Thiol-blocking electrophiles interfere with labeling and detection of protein sulfenic acids. *FEBS Journal* 280, 6150–6161 (2013).
16. Dóka *et al.* Control of protein function through oxidation and reduction of persulfidated states. *Sci Adv* 6, (2020).
17. Yang, J., Gupta, V., Carroll, K. S. & Liebler, D. C. Site-specific mapping and quantification of protein S-sulphenylation in cells. *Nat Commun* 5, 4776 (2014).
18. Fu, L., Liu, K., Ferreira, R. B., Carroll, K. S. & Yang, J. Proteome-Wide Analysis of Cysteine S-Sulfenylation Using a Benzothiazine-Based Probe. *Curr Protoc Protein Sci* 95, e76 (2019).
19. He, J.-X. *et al.* A modification-centric assessment tool for the performance of chemoproteomic probes. *Nat Chem Biol* 18, 904–912 (2022).
20. Gupta, V., Yang, J., Liebler, D. C. & Carroll, K. S. Diverse Redoxome Reactivity Profiles of Carbon Nucleophiles. *J Am Chem Soc* 139, 5588–5595 (2017).
21. Binns, D. *et al.* QuickGO: a web-based tool for Gene Ontology searching. *Bioinformatics* 25, 3045–3046 (2009).
22. Sherman, B. T. *et al.* DAVID: a web server for functional enrichment analysis and functional annotation of gene lists (2021 update). *Nucleic Acids Res* 50, W216–W221 (2022).
23. Huang, D. W., Sherman, B. T. & Lempicki, R. A. Systematic and integrative analysis of large gene lists using DAVID bioinformatics resources. *Nat Protoc* 4, 44–57 (2009).
24. Supek, F., Bošnjak, M., Škunca, N. & Šmuc, T. REVIGO Summarizes and Visualizes Long Lists of Gene Ontology Terms. *PLoS One* 6, e21800 (2011).
25. Fu, L. *et al.* Direct Proteomic Mapping of Cysteine Persulfidation. *Antioxid Redox Signal* 33, 1061–1076 (2020).
26. Kelmer Sacramento, E. *et al.* Reduced proteasome activity in the aging brain results in ribosome stoichiometry loss and aggregation. *Mol Syst Biol* 16, 1–22 (2020).
27. Bibli, S. I. *et al.* Mapping the Endothelial Cell S -Sulfhydrome Highlights the Crucial Role of Integrin Sulfhydration in Vascular Function. *Circulation* 143, 935–948 (2021).
28. Shen, X. *et al.* Nonlinear dynamics of multi-omics profiles during human aging. *Nat Aging* 4, 1619–1634 (2024).
29. Hine, C. *et al.* Endogenous Hydrogen Sulfide Production Is Essential for Dietary Restriction Benefits. *Cell* 160, 132–144 (2015).
30. Sbodio, J. I., Snyder, S. H. & Paul, B. D. Transcriptional control of amino acid homeostasis is disrupted in Huntington's disease. *Proceedings of the National Academy of Sciences* 113, 8843–8848 (2016).

31. Ding, J. *et al.* A metabolome atlas of the aging mouse brain. *Nat Commun* 12, 6021 (2021).
32. Schaum, N. *et al.* Ageing hallmarks exhibit organ-specific temporal signatures. *Nature* 583, 596–602 (2020).
33. Hernandez, D. G. *et al.* Integration of GWAS SNPs and tissue specific expression profiling reveal discrete eQTLs for human traits in blood and brain. *Neurobiol Dis* 47, 20–28 (2012).
34. Lamprianou, S., Chatzopoulou, E., Thomas, J.-L., Bouyain, S. & Harroch, S. A complex between contactin-1 and the protein tyrosine phosphatase PTPRZ controls the development of oligodendrocyte precursor cells. *Proceedings of the National Academy of Sciences* 108, 17498–17503 (2011).
35. Storici, P., Capitani, G., Müller, R., Schirmer, T. & Jansonius, J. N. Crystal structure of human ornithine aminotransferase complexed with the highly specific and potent inhibitor 5-fluoromethylornithine 1 1 1Edited by R. Huber. *J Mol Biol* 285, 297–309 (1999).
36. Hoelz, A., Nairn, A. C. & Kuriyan, J. Crystal Structure of a Tetradecameric Assembly of the Association Domain of Ca2+/Calmodulin-Dependent Kinase II. *Mol Cell* 11, 1241–1251 (2003).
37. Huyton, T. *et al.* The crystal structure of murine p97/VCP at 3.6Å. *J Struct Biol* 144, 337–348 (2003).
38. Margreitter, C., Petrov, D. & Zagrovic, B. Vienna-PTM web server: a toolkit for MD simulations of protein post-translational modifications. *Nucleic Acids Res* 41, 422–426 (2013).
39. Poynton, R. A. & Hampton, M. B. Peroxiredoxins as biomarkers of oxidative stress. *Biochim Biophys Acta Gen Subj* 1840, 906–912 (2014).
40. Kinumi, T., Kimata, J., Taira, T., Ariga, H. & Niki, E. Cysteine-106 of DJ-1 is the most sensitive cysteine residue to hydrogen peroxide-mediated oxidation in vivo in human umbilical vein endothelial cells. *Biochem Biophys Res Commun* 317, 722–728 (2004).
41. Li, P. *et al.* High-throughput and proteome-wide discovery of endogenous biomolecular condensates. *Nat Chem* 16, 1101–1112 (2024).
42. Milovanovic, D., Wu, Y., Bian, X. & De Camilli, P. A liquid phase of synapsin and lipid vesicles. *Science* 361, 604–607 (2018).
43. Gupta, V., Paritala, H. & Carroll, K. S. Reactivity, Selectivity, and Stability in Sulfenic Acid Detection: A Comparative Study of Nucleophilic and Electrophilic Probes. *Bioconjug Chem* 27, 1411–1418 (2016).
44. Filipovic, M. R., Zivanovic, J., Alvarez, B. & Banerjee, R. Chemical Biology of H2S Signaling through Persulfidation. *Chem Rev* 118, 1253–1337 (2018).
45. Gupta, V. & Carroll, K. S. Sulfenic acid chemistry, detection and cellular lifetime. *Biochim Biophys Acta Gen Subj* 1840, 847–875 (2014).
46. Shi, Y. & Carroll, K. S. Activity-Based Sensing for Site-Specific Proteomic Analysis of Cysteine Oxidation. *Acc Chem Res* 53, 20–31 (2020).
47. Dóka, É. *et al.* A novel persulfide detection method reveals protein persulfide- and polysulfide-reducing functions of thioredoxin and glutathione systems. *Sci Adv* 2, e1500968 (2016).
48. Dóka *et al.* Control of protein function through oxidation and reduction of persulfidated states. *Sci Adv* 6, (2020).
49. Zhang, D. *et al.* Detection of Protein S-Sulfhydration by a Tag-Switch Technique. *Angewandte Chemie International Edition* 53, 575–581 (2014).

50. Zivanovic, J. *et al.* Selective Persulfide Detection Reveals Evolutionarily Conserved Antiaging Effects of S-Sulfhydration. *Cell Metab* 30, 1152-1170.e13 (2019).
51. Li, P. *et al.* High-throughput and proteome-wide discovery of endogenous biomolecular condensates. *Nat Chem* 16, 1101–1112 (2024).
52. Kato, M. *et al.* Redox State Controls Phase Separation of the Yeast Ataxin-2 Protein via Reversible Oxidation of Its Methionine-Rich Low-Complexity Domain. *Cell* 177, 711-721.e8 (2019).
53. Abe, K. & Kimura, H. The possible role of hydrogen sulfide as an endogenous neuromodulator. *J Neurosci* 16, 1066–1071 (1996).
54. Kamat, P. K., Kalani, A. & Tyagi, N. Role of hydrogen sulfide in brain synaptic remodeling. *Methods Enzymol* 555, 207–229 (2015).
55. Ali, R., Pal, H. A., Hameed, R., Nazir, A. & Verma, S. Controlled release of hydrogen sulfide significantly reduces ROS stress and increases dopamine levels in transgenic C. elegans. *Chem. Commun.* 55, 10142–10145 (2019).
56. Molliex, A. *et al.* Phase Separation by Low Complexity Domains Promotes Stress Granule Assembly and Drives Pathological Fibrillization. *Cell* 163, 123–133 (2015).
57. Sanders, D. W. *et al.* Competing Protein-RNA Interaction Networks Control Multiphase Intracellular Organization. *Cell* 181, 306-324.e28 (2020).
58. Yang, P. *et al.* G3BP1 Is a Tunable Switch that Triggers Phase Separation to Assemble Stress Granules. *Cell* 181, 325-345.e28 (2020).
59. Guillén-Boixet, J. *et al.* RNA-Induced Conformational Switching and Clustering of G3BP Drive Stress Granule Assembly by Condensation. *Cell* 181, 346-361.e17 (2020).
60. Kato, M. *et al.* Cell-free formation of RNA granules: Low complexity sequence domains form dynamic fibers within hydrogels. *Cell* 149, 753–767 (2012).
61. Banani, S. F. *et al.* Compositional Control of Phase-Separated Cellular Bodies. *Cell* 166, 651–663 (2016).
62. Wolozin, B. & Ivanov, P. Stress granules and neurodegeneration. *Nat Rev Neurosci* 20, 649–666 (2019).
63. Khong, A. *et al.* The Stress Granule Transcriptome Reveals Principles of mRNA Accumulation in Stress Granules. *Mol Cell* 68, 808-820.e5 (2017).
64. Kennedy, D. *et al.* Characterization of G3BPs: Tissue specific expression, chromosomal localisation and rasGAP120 binding studies. *J Cell Biochem* 84, 173–187 (2002).
65. Jacob, M. H., Amir, D., Ratner, V., Gussakowsky, E. & Haas, E. Predicting Reactivities of Protein Surface Cysteines as Part of a Strategy for Selective Multiple Labeling. *Biochemistry* 44, 13664–13672 (2005).
66. Cuevasanta, E. *et al.* Reaction of Hydrogen Sulfide with Disulfide and Sulfenic Acid to Form the Strongly Nucleophilic Persulfide. *Journal of Biological Chemistry* 290, 26866–26880 (2015).
67. Filipovic, M. R., Zivanovic, J., Alvarez, B. & Banerjee, R. Chemical Biology of H2S Signaling through Persulfidation. *Chem Rev* 118, 1253–1337 (2018).
68. Vitvitsky, V., Kabil, O. & Banerjee, R. High Turnover Rates for Hydrogen Sulfide Allow for Rapid Regulation of Its Tissue Concentrations. *Antioxid Redox Signal* 17, 22–31 (2012).
69. Wedmann, R. *et al.* Working with ‘H2S’: Facts and apparent artifacts. *Nitric Oxide* 41, 85–96 (2014).

70. Petrovic, D. *et al.* Ergothioneine improves healthspan of aged animals by enhancing cGPDH activity through CSE-dependent persulfidation. *Cell Metab* 37, 542-556.e14 (2025).
71. Wolozin, B. & Ivanov, P. Stress granules and neurodegeneration. *Nat Rev Neurosci* 20, 649–666 (2019).
72. Alberti, S. & Hyman, A. A. Biomolecular condensates at the nexus of cellular stress, protein aggregation disease and ageing. *Nat Rev Mol Cell Biol* 22, 196–213 (2021).
73. Banani, S. F., Lee, H. O., Hyman, A. A. & Rosen, M. K. Biomolecular condensates: Organizers of cellular biochemistry. *Nat Rev Mol Cell Biol* 18, 285–298 (2017).
74. Laferrière, F. *et al.* TDP-43 extracted from frontotemporal lobar degeneration subject brains displays distinct aggregate assemblies and neurotoxic effects reflecting disease progression rates. *Nat Neurosci* 22, 65–77 (2019).
75. Jo, M. *et al.* The role of TDP-43 propagation in neurodegenerative diseases: integrating insights from clinical and experimental studies. *Exp Mol Med* 52, 1652–1662 (2020).
76. Yan, X. *et al.* Intra-condensate demixing of TDP-43 inside stress granules generates pathological aggregates. *Cell* 188, 4123-4140.e18 (2025).
77. Cairns, N. J. *et al.* TDP-43 in Familial and Sporadic Frontotemporal Lobar Degeneration with Ubiquitin Inclusions. *Am J Pathol* 171, 227–240 (2007).
78. Gasset-Rosa, F. *et al.* Cytoplasmic TDP-43 De-mixing Independent of Stress Granules Drives Inhibition of Nuclear Import, Loss of Nuclear TDP-43, and Cell Death. *Neuron* 102, 339-357.e7 (2019).
79. Patel, B. H., Percivalle, C., Ritson, D. J., Duffy, C. D. & Sutherland, J. D. Common origins of RNA, protein and lipid precursors in a cyanosulfidic protometabolism. *Nat Chem* 7, 301–307 (2015).
80. Foden, C. S. *et al.* Prebiotic synthesis of cysteine peptides that catalyze peptide ligation in neutral water. *Science (1979)* 370, 865–869 (2020).
81. Fox, S. W. The evolutionary significance of phase-separated microsystems. *Orig Life* 7, 49–68 (1976).
82. Spruijt, E. Open questions on liquid–liquid phase separation. *Commun Chem* 6, 1–5 (2023).
83. Principles, P. NASA Public Access. 57, 2509–2519 (2020).
84. Balaban, R. S., Nemoto, S. & Finkel, T. Mitochondria, oxidants, and aging. *Cell* 120, 483–495 (2005).
85. Van Raamsdonk, J. M. & Hekimi, S. Reactive oxygen species and aging in caenorhabditis elegans: Causal or casual relationship? *Antioxid Redox Signal* 13, 1911–1953 (2010).
86. Knoefler, D. *et al.* Quantitative In Vivo Redox Sensors Uncover Oxidative Stress as an Early Event in Life. *Mol Cell* 47, 767–776 (2012).
87. Bazopoulou, D. *et al.* Developmental ROS individualizes organismal stress resistance and lifespan. *Nature* 576, 301–305 (2019).
88. Redman, L. M. *et al.* Metabolic Slowing and Reduced Oxidative Damage with Sustained Caloric Restriction Support the Rate of Living and Oxidative Damage Theories of Aging. *Cell Metab* 27, 805-815.e4 (2018).
89. Sánchez Milán, J. A. *et al.* Trioxidized cysteine in the aging proteome mimics the structural dynamics and interactome of phosphorylated serine. *Aging Cell* 23, (2024).

90. Jahn, R., Cafiso, D. C. & Tamm, L. K. Mechanisms of SNARE proteins in membrane fusion. *Nat Rev Mol Cell Biol* https://doi.org/10.1038/s41580-023-00668-x (2023) doi:10.1038/s41580-023-00668-x.
91. Hoffmann, C. *et al.* Synapsin condensation controls synaptic vesicle sequestering and dynamics. *Nat Commun* 14, 6730 (2023).
92. Cao, X., Jin, X. & Liu, B. The involvement of stress granules in aging and aging-associated diseases. *Aging Cell* 19, 1–20 (2020).
93. Smotrys, J. E. & Linder, M. E. Palmitoylation of Intracellular Signaling Proteins: Regulation and function. *Annu Rev Biochem* 73, 559–587 (2004).
94. Zuhra, K. *et al.* Endogenously produced hydrogen cyanide serves as a novel mammalian gasotransmitter. *Nat Metab* in press, (2025).
95. Qin, W. *et al.* S-glycosylation-based cysteine profiling reveals regulation of glycolysis by itaconate. *Nat Chem Biol* 15, 983–991 (2019).
96. Yau, Y. F. *et al.* Investigating the efficacy of ergothioneine to delay cognitive decline in mild cognitively impaired subjects: A pilot study. *Journal of Alzheimer's Disease* 102, 841–854 (2024).
97. Perez-Riverol, Y. *et al.* The PRIDE database at 20 years: 2025 update. *Nucleic Acids Res* 53, D543–D553 (2025).
98. Hartley, M. *et al.* The BioImage Archive – Building a Home for Life-Sciences Microscopy Data. *J Mol Biol* 434, 167505 (2022).
99. Yang, G. *et al.* H2S as a physiologic vasorelaxant: Hypertension in mice with deletion of cystathionine γ-lyase. *Science (1979)* 322, 587–590 (2008).
100. Karpievitch, Y. V. *et al.* Normalization of peak intensities in bottom-up MS-based proteomics using singular value decomposition. *Bioinformatics* 25, 2573–2580 (2009).
101. Tyanova, S. *et al.* The Perseus computational platform for comprehensive analysis of (prote)omics data. *Nature Methods* vol. 13 731–740 Preprint at https://doi.org/10.1038/nmeth.3901 (2016).
102. Kanehisa, M., Furumichi, M., Tanabe, M., Sato, Y. & Morishima, K. KEGG: new perspectives on genomes, pathways, diseases and drugs. *Nucleic Acids Res* 45, D353–D361 (2017).
103. Aleksander, S. A. *et al.* The Gene Ontology knowledgebase in 2023. *Genetics* 224, (2023).
104. Ashburner, M. *et al.* Gene Ontology: tool for the unification of biology. *Nat Genet* 25, 25–29 (2000).
105. Shevchenko, A., Tomas, H., Havliš, J., Olsen, J. V. & Mann, M. In-gel digestion for mass spectrometric characterization of proteins and proteomes. *Nat Protoc* 1, (2007).
106. Hoffmann, C. *et al.* Synapsin Condensates Recruit alpha-Synuclein. *J Mol Biol* 433, 166961 (2021).
107. Ellman, G. L. Tissue sulfhydryl groups. *Arch Biochem Biophys* 82, 70–77 (1959).
108. Gupta, V. & Carroll, K. S. Profiling the reactivity of cyclic C-nucleophiles towards electrophilic sulfur in cysteine sulfenic acid. *Chem Sci* 7, 400–415 (2016).
109. Liu, H. & Naismith, J. H. An efficient one-step site-directed deletion, insertion, single and multiple-site plasmid mutagenesis protocol. *BMC Biotechnol* 8, (2008).
110. Kong, A. T., Leprevost, F. V., Avtonomov, D. M., Mellacheruvu, D. & Nesvizhskii, A. I. MSFragger: Ultrafast and comprehensive peptide

identification in mass spectrometry-based proteomics. *Nat Methods* 14, 513–520 (2017).
111. Gozzi, G. J. *et al.* Selecting the first chemical molecule inhibitor of HSP110 for colorectal cancer therapy. *Cell Death Differ* 27, 117–129 (2020).
112. Krajewski, W. W. *et al.* Crystal Structures of Mammalian Glutamine Synthetases Illustrate Substrate-Induced Conformational Changes and Provide Opportunities for Drug and Herbicide Design. *J Mol Biol* 375, 217–228 (2008).
113. Paithankar, K. S., Rittner, A., Vu Huu, K. & Grininger, M. KS-MAT DI-DOMAIN OF MOUSE FAS. Preprint at https://doi.org/10.2210/pdb5my2/pdb (2018).
114. Jumper, J. *et al.* Highly accurate protein structure prediction with AlphaFold. *Nature* 596, 583–589 (2021).

Acknowledgments: We thank Ingo Feldman and Susanne Krois (ISAS e.V.) for their technical assistance with MS and the Advanced Medical Bioimaging Core Facility at Charité for the support.

Funding: This study was funded by European Research Council (ERC) under the European Union's Horizon 2020 research and innovation programme (Grant Agreement No. 864921). The authors also acknowledge support from the start-up funds from DZNE, the grants from the German Research Foundation (SFB 1286/B10 and MI 2104), and the Human Frontiers Science Organization (RGEC32/2023) (to DM), the Hellenic Foundation for Research and Innovation (HFRI-FM17-886) (to AP), the Medical Research Council UK (MC_UU_00028/4 to MPM and MC_UU_00028/5 for JP) and by a Wellcome Trust Investigator award (220257/Z/20/Z) (to MPM), and Ministry of Science, Technological Development and Innovation of Republic of Serbia, Contract number: 451-03-136/2025-03/200168 (to NP). CH is supported by a fellowship of the Innovative Minds Program of the German Dementia Association; HW is supported by the Oversea Study Program of Guangzhou Elite Project (SJ2020/2/JY202025). B.D.P. and A.A.P. are supported by the American Heart Association and Paul Allen Foundation grant 19PABH134580006 and R01AG071512. B.D.P. is also supported by NIH NIDA, grants P50 DA044123, NIH NIA 1R21AG073684 and funding from the Solve-ME foundation and the Catalyst Award from Johns Hopkins University. A.A.P. is supported by The Valour Foundation and as the Case Western Reserve University Rebecca E. Barchas, M.D., D.L.F.A.P.A. University Professor in Translational Psychiatry and the University Hospitals Morley–Mather Chair in Neuropsychiatry. A.A.P. also acknowledges support from Department of Veterans Affairs Merit Award I01BX005976, NIH/NIGMS RM1 GM142002, NIH/NIA

RO1AG066707, NIH/NIA 1 U01 AG073323, and NIH/NIA 1 P30 AGO62428-01, and the Louis Stokes VA Medical Center resources and facilities.

Competing interests: Authors declare that they have no competing interests.

Data and materials availability: All raw data that are not included in this study will be available on Mendeley repository. All proteomic data are available through PRIDE[97] under code numbers: **PXD045785** (Sulfenylome and total proteome; **Username:** reviewer_pxd045785@ebi.ac.uk, **Password:** GM9xPMNV); **PXD045806** (Persulfidation and Sulfonylation; **Username:** reviewer_pxd045806@ebi.ac.uk, **Password:** tsLiiy21); **PXD045820** (TPP of WT and *Cse*$^{-/-}$ MEFs upon H_2O_2 stress; reviewer_pxd045820@ebi.ac.uk, **Password:** 2OElzAoK). Galyas silver staining images of 18-month-old WT and *Cse*$^{-/-}$ are available on BioImage Archive[98] repository (DOI: 10.6019\\S-BIAD1604; https://www.ebi.ac.uk/biostudies/bioimages/studies/S-BIAD1604?key=2c830e02-9dfe-429f-a38f-fbe2336e7326). An online platform for interactive data exploration: **https://aging-redox-proteomics-viewer.streamlit.app/**. The site is currently password-protected (username: reviewer.app; password: Ycql59H3s621).

Declaration of interests: MRF is a member of Scientific Advisory Board of MitoRx Therapeutics.

Methods

Mice

Wild-type and *Cse* KO animals[99] were bred/housed in ventilated cages, under specific pathogen-free, temperature controlled (22 °C) and 12 h light/dark cycle conditions in full compliance with the guidelines of the Federation of Laboratory Animal Science Association recommendations in the Laboratory Animal Unit of Biomedical Research Foundation of the Academy of Athens (BRFAA) and allowed unrestricted access to chow diet and water. All studies were performed on male mice at the indicated age.

Cell culture

Cse$^{-/-}$ mouse embryonic fibroblasts (MEF) were from Professor Bindu Paul (Johns Hopkins University) and were generated from *Cse*$^{+/+}$ and *Cse*$^{-/-}$ mice and immortalized using SV40T antigen.[30] MEF cells were cultured in DMEM, supplemented with 2 mM L-glutamine, 1 % penicillin-streptomycin, and 10 % fetal bovine serum at 37 °C and 5 % CO2. Human primary fibroblasts (AG1449 (48 yo) AG16359 (79 yo)) were obtained from the Coriell Institute for Medical Research. Cells were cultured following the same conditions used for MEFs, with the exception that no antibiotics were added to the medium. The striatal progenitor cell line *STHdh*$^{Q7/Q7}$, expressing wild-type huntingtin,

and *STHdh*$^{Q111/Q111}$, expressing mutant huntingtin harboring 111 glutamine repeats (referred to as Q7 and Q111 cells, respectively) were maintained in DMEM (low glucose, no pyruvate) supplemented with 2 mM L-glutamine, 1 % penicillin-streptomycin, and 10 % fetal bovine serum at 33 °C and 5 % CO_2.

Persulfidation enrichment for proteomic analysis

The brain frontal cortexes were lysed in cold HEN Buffer (50 mM HEPES, 1 mM EDTA, 0.1 mM neocuproine, 1 % IGEPAL, 2 % SDS, pH 7.4) supplemented with 5 mM 4-Chloro-7-nitrobenzofurazan (NBF-Cl). Frozen tissue was disrupted in lysis buffer using the TissueLyser II (Qiagen) and 5 mm stainless steel beads. Persulfidation enrichment was performed using previously described method.[4] Enriched proteins were eluted by incubating beads with 2.25 M ammonia solution for 16 h and collected the following morning for lyophilization. Lyophilized samples were dissolved in digestion buffer (50 mM ammonium bicarbonate [ABC], 1 mM calcium chloride) and digested overnight using trypsin at trypsin:protein ratio 1:20. The desalting was performed on Supel™-Select HLB SPE Tube. Eluates were evaporated under vacuum until dryness. Peptides were dissolved in 0.1 % TFA, and digestion and desalting quality control was performed using an Dionex UltiMate 3000 (RSLC) system with a PepSwift Monolithic® Trap 200 µm * 5 mm (Thermo Fisher Scientific).

Sulfenylation enrichment for proteomic analysis

Brain frontal cortexes were lysed in cold HEN Buffer supplemented with 0.5 mM Benzo[c][1,2]thiazine-based BTD (BTD) synthesized in house following established protocol.[20] Lysates were incubated for 2 h at 37 °C followed by two methanol/chloroform precipitations. The sulfenylation enrichment was carried out using a modified method from Fu et al, 2019.[18] Shortly, samples were resuspended in HEPES + 2 % SDS and treated with 10 mM DTT for 1 h at 37 °C, followed by 40 mM iodoacetamide (IAM) for 30 min at RT. Excess DTT and IAM were removed by methanol chloroform precipitation, and proteins were resuspended in 50 mM HEPES pH 7.0, 2 % SDS. 1.5 mg of proteins were incubated for 2 h at 37 °C with 0.2 mM Az-UV-Cleavable-biotin, 1 mM Ascorbic acid, and 0.1 mM Copper-TBTA to perform the click-chemistry reaction. Precipitated proteins were dissolved in neutravidin Binding buffer (50 mM NaOAc, pH 4.5) and 0.2 % SDS. Protein concentration was performed, and 0.9 mg of proteins were incubated with Pierce™ High Capacity NeutrAvidin Agarose beads. After 3 h of mixing at RT, beads were loaded onto columns and washed with neutravidin washing buffer (50 mM NaOAc and 2 M NaCl, pH 4.5). Sulfenylated proteins were then released by incubating beads for 3 h under UV light (365 nm) in 25 mM ammonium bicarbonate buffer. Supernatants were collected and lyophilized. Samples were then digested and desalted as detailed above. Peptides were dissolved in 0.1 % TFA, and digestion quality control was performed as described.

LC/MS analysis

Persulfidome

Peptides were dissolved in 0.1% TFA before being analyzed by high-resolution LC-MS/MS using an Ultimate 3000 Nano Ultra High-Pressure Chromatography (UPLC) system (Thermo Fisher Scientific) coupled with a Thermo LTQ Velos Mass Spectrometer via an EASY-spray (Thermo Fisher Scientific). Peptide separation was carried out with an Acclaim™ PepMap™ 100 C18 column (Thermo Fisher Scientific)

using a 140 min non-linear gradient from 7 to 80% B (0 min, 7% B; 15 min 17% B; 30 min, 30% B; 120 min, 65% B; 140 min 80% B; B:84% Acetonitrile, 0.1% Formic Acid) at a flow rate of 250 nL/min. The LTQ Velos was operated in a DDA mode, and MS1 survey scans were acquired from m/z 300 to 2000 at a resolution of 60 000 using the Orbitrap mode. The ten most intense peaks with a charge state ≥ 2 were fragmented using Collision-induced dissociation (CID) set at 35% and fragmentation analyzed using Iontrap at a standard scan rate. The dynamic exclusion was set at 20 seconds.

Sulfenylome

Peptides were analyzed by high-resolution LC-MS/MS using an Dionex UltiMate 3000 RSLC Systems (RSLC) system (Thermo Fisher Scientific) coupled with an Orbitrap Eclipse™ Tribrid™ Mass Spectrometer via an EASY-spray (Thermo Fisher Scientific). Peptide separation was carried out with an Acclaim™ PepMap™ 100 C18 column (Thermo Fisher Scientific) using a 65 min linear gradient from 3 to 35 % of B (84 % Acetonitrile, 0.1 % Formic Acid) at a flow rate of 250 nL/min. The Orbitrap Eclipse™ was operated in a DDA mode, and MS1 survey scans were acquired from m/z 300 to 1,500 at a resolution of 120,000 using the Orbitrap mode. MS2 scans were carried out for 3 seconds with high-energy collision-induced dissociation (HCD) at 32 % using the Normal speed IonTrap mode.

Data were evaluated with PEAKS ONLINE software using 15 ppm for precursor mass tolerance, 0.5 Da for fragment mass tolerance, specific tryptic digest, and a maximum of 3 missed cleavages. For persulfidation detection, NBF (+163.00961594 Da) on C, K, R, DCP (+168.0786442 Da) on C, N-term acetylation (+42.010565 Da), and methionine oxidation (+15.994915 Da) were added as variable modifications. For sulfenylation detection, BTD–UV-cleavable probe (cleaved, +418.1311 Da), carbamidomethylation (+57.021464 Da) on C, N-term acetylation (+42.010565 Da), and methionine oxidation (+15.994915 Da) were added as variable modifications, peptide-spectrum match (PSM) and proteins were filtered at FDR 1 %. Quantification was carried out at the MS1 levels and match between run (MBR) function with default filtering parameters was used. Proteins with at least 1 unique peptide were considered for quantification.

Total proteome analysis

Brain frontal cortexes were disrupted in lysis buffer (50 mM TRIS, 150 mM NaCl, 2% SDS, 1% IGEPAL, pH 7.8) using the Tissuelyser II and twenty 1.4 mm ceramic beads (Qiagen, #13113). Lysates were incubated with Benzonase following manufacturer recommendation for 30 min and precipitated. Samples were then resuspended in 50 mM HEPES, 2 % SDS, and incubated with 10 mM DTT at RT followed by incubation with 50 mM IAM for 1h at 37°C. Precipitation was used to stop the reaction and concentrate proteins. For tryptic digestion, samples were resuspended in 6 M guanidine hydrochloride.250 µg of protein were digested overnight at 37 °C using trypsin with a 1:20 trypsin to sample ratio (Promega, #V5117). The next day, peptides were desalted evaporated under vacuum until dryness as described above.

Peptides were dissolved in 0.1 % TFA, and digestion quality control was performed as described above. Peptides were analyzed by high-resolution LC-MS/MS using an Dionex UltiMate 3000 (RSLC) Systems (Thermo Fisher Scientific) coupled to a timsTOF Pro (Bruker) equipped with a CaptiveSpray source. Peptide separation was carried out with an Acclaim™ PepMap™ 100 C18 column (Thermo Fisher Scientific) using a 65 min linear gradient from 3 to 35 % of B (84 % Acetonitrile, 0.1 % Formic Acid) at a flow rate of 250 nL/min. The timsTOF Pro (Bruker) was operated in PASEF

mode using Compass Hystar 5.0.36.0. The TIMS setting was as follows: Mass Range 100 to 1700 m/z, 1/K0 Start 1.6 Vs/cm2 End 1.6 Vs/cm2, Ramp time 100 ms, Lock Duty Cycle to 100 %, Capillary Voltage 1500V, Dry Gas 3 l/min, Dry Temp 180°C. PASEF settings: 10 MS/MS scans, charge range 0-5, active exclusion for 0.4 min, Scheduling Target intensity 20000, Intensity threshold 2500, CID collision energy 49 eV.

Data were evaluated with PEAKS ONLINE software using 20 ppm for precursor mass tolerance, 0.5 Da for fragment mass tolerance, specific tryptic digest, and a maximum of 3 missed cleavages. Carbamidomethylation (+57.021464 Da) on C, N-term acetylation (+42.010565 Da), and methionine oxidation (+15.994915 Da) were added as variable modifications, PSM and proteins were filtered at FDR 1 %. Data were normalized based on the total ion count (TIC). Quantification was carried out at the MS1 levels and match between run (MBR) function with default filtering parameters was used. Proteins with at least 1 unique peptide were considered for quantification.

Direct detection of Sufonylated (SO_3H) peptides using LC/MS

50 µg of the NBF-labelled samples dissolved in PBS 2 % SDS (see section “PSSH enrichment for proteomic analysis”) were trypsinized overnight as described above. Samples were subjected to desalting and Pierce® Detergent Removal columns (ThermoFisher, # 87777). Peptides evaporated under vacuum until dryness as described above.

Peptides were dissolved in 0.1 % TFA, and digestion quality was assessed as previously described. Peptides were analyzed by high-resolution LC-MS/MS using Dionex UltiMate 3000 RSLC Systems (RSLC) system (Thermo Fisher Scientific) coupled with an Orbitrap Eclipse™ Tribrid™ Mass Spectrometer via an EASY-spray (Thermo Fisher Scientific). Peptide separation was carried out with an Acclaim™ PepMap™ 100 C18 column using a 160 min linear gradient from 3 to 35 % of B (84 % Acetonitrile, 0.1 % Formic Acid) at a flow rate of 250 nL/min. Parameters were set as described above.

Data were evaluated with PEAKS ONLINE software using 15 ppm for precursor mass tolerance, 0.5 Da for fragment mass tolerance, specific tryptic digest, and a maximum of 3 missed cleavages. NBF (+163.00961594 Da) on C, K, and R, 'Cysteine oxidation to cysteic acid' (-SO_3H, +47.984745 Da, Unimod ID: 345) on C, N-term acetylation (+42.010565 Da), and methionine oxidation (+15.994915 Da) were added as variable modifications, PSM and proteins were filtered at FDR 1 %.

Proteomic bioinformatic analysis

Persulfidation and Sulfenylation

Persulfidation and sulfenylation dataset were search against the UNIPROT mouse database and filtered at 3 out 4 and 2 out 3 quantifiable values per group respectively. Datasets were further filtered for protein that are containing at least one cysteine to avoid false discovery and normalized using EigenMS R script.[100] Each group were then tested against each other using Welsch´s test and p-value was corrected using permutation-based FDR. All statistical tests were performed using Perseus.[101] Protein with FDR adjusted p-value ≤ 0.05 and with a fold change higher than 30% were considered as significantly changing and were used for downstream analysis.

KEGG pathway enrichment[102] and GO term enrichment analysis[103,104] were performed against the whole mouse genome background already integrated in DAVID bioinformatics webtool.[22,23] Visualization of KEGG enrichment and GO term were

performed using in-house built R script. Further semantic space analysis of GO term enrichment was performed using the REVIGO webtool[24] and plotted on R.

Protein localization was retrieved using QuickGO[21] and searched against seven localizations from GO slims (cytoskeleton, Golgi apparatus, plasma membrane, nucleus, cytosol, endoplasmic reticulum and mitochondrion). Protein with multiple localization were included in all the compartments associated to it.

Correlation scatter plots and kernel density estimations were generated using an in-house Python script.

Total proteome

The total proteome search was performed against the Uniprot mouse database and filtered at 3 out 4 quantifiable values and normalized by total ion count (TIC). Statistical tests were performed as described above for the persulfidation and sulfenylation datasets. Proteins were considered as significantly changing when adjusted p-value <0.05 and the fold change was ≥ 50%. Downstream analysis was performed as described previously.

Sulfonylated cysteine peptide analysis

Quantification of sulfonylated peptides was performed following protocols recently developed for protein cyanylation.[94] Quantifiable sulfonylated cysteine peptides were filtered for 3 out of 4 valid values for each group and in addition, protein quantification of the dataset was performed. For each protein, the ratio of the mean value of each group was used to normalize the peptide quantification. For each peptide, the sulfonylated cysteine position in the protein was retrieved using an in-house R script. Furthermore, peptides exclusively present in WT 18 months or *Cse*$^{-/-}$ 10 weeks ≥ 3 out of 4 values, were extracted and presented in a separate excel sheet.

Immunoblotting

Cells or tissues were lysed in HEN buffer supplemented with 20 mM IAM and incubated at 37°C for 2 h to allow complete cysteine blocking. The excess of blocking-reagent was removed by precipitation, as mentioned above. The samples were then resuspended in HEPES + 2 % SDS and readjusted using DC™ protein assay. One equivalent of Laemmli (4X) buffer supplemented with 10 % β-mercaptoethanol was added to three sample equivalents for SDS-PAGE and boiled at 95 °C for 5 min protected from light. Equal amounts of proteins were resolved by SDS-page using standard protocol. Samples were then immunoblotted with the indicated antibodies and dilutions; (anti-Prdx-SO3 [Abcam, #ab16830], 1:4000; anti-oxDJ-1 [Sigma-Aldrich, #MABN1773], 1:2000; anti- GAPDH-SO3 [Abfrontier, #LF-PA0006], 1:2000; anti-GAPDH-AF488 [Sigma-Aldrich, #MAB374-AF488],1:20000; Rabbit anti-Cth [Proteintech®, 12217-1-AP], 1:1000; Mouse anti-Cth [Santa Cruz Biotechnology, INC.; sc-374249], 1:750; anti-eIF2α 1 [Invitrogen, AHO0802], 1:1000; anti-phopho-eIF2α [GeneTex, GTX24837], 1:2000; anti-TDP43 [Proteintech®, 10782-2-AP], 1:1000; anti-β-Tubulin [Sigma-Aldrich, #T0198], 1:5000; anti-Rabbit- AF680 [Abcam, #ab175773], 1:20000; anti-Mouse-AF680 [Abcam, #ab175775], 1:20000).

Filter trap assay

Cell lines

MEFs or STHdh cells were harvested by scraping in cold PBS. Lysis was carried out by liquid homogenization with a 23G needle and syringe in filter trap lysis buffer (150mM NaCl, 50 mM Hepes, 1mM EDTA, 1% TritonX-100, protease inhibitors

(cOmplete™, Mini, EDTA-free Protease Inhibitor Cocktail, Roche). Protein concentration was determined using the Pierce BCA assay (23227 Thermo Fisher Scientific) and 0.5% SDS (final concentration) was added to the samples. Acetate cellulose blotting membrane (Cytiva OE66 10404180) and Whatman filter paper were pre-soaked in PBS and equilibrated by 3 washes in lysis buffer containing 0.5% SDS following cassette assembly. After loading of 120 µg of protein, the membrane was washed 5 times in lysis buffer containing 0.2% SDS followed by standard immunoblotting. The membrane was probed with anti-TDP43-AF790 (1:500 [Santa Cruz Biotechnology, INC.; sc-376311] and anti-G3BP2, (1:600 [Proteintech®, 16276-1-AP]), followed by mouse anti-rabbit IgG-CFL 488 [Santa Cruz Biotechnology, INC.; sc-516248]). Equal loading was ensured by SDS-PAGE followed by immunoblotting using anti-GAPDH(6C5)-AF488 (Merck, MAB374).

Brain tissue

Brain frontal cortexes from WT and *Cse*$^{-/-}$ at 18 months were lysed in cold filter trap lysis Buffer. Disruption of frozen tissue was carried out in lysis buffer using the Omni Bead Ruptor 12 bead mill homogeniser (Camlab) and 1.4mm ceramic beads. Lysates were centrifuged at 2,000 × *g* for 10 minutes at 4 °C. The filter trap assay was then performed as described for the cell lines. The membranes were probed with anti-TDP43-AF790 (1:500 [Santa Cruz Biotechnology, INC.; sc-376311], anti-TIA-1/TIAR(D-9)AF-647 (1:250 [Santa Cruz Biotechnology, INC.; sc-48371]), anti-GAPDH(6C5)-AF488 (1:250 Merck, MAB374) and mouse anti-Tau(D-8) (1:300 [Santa Cruz Biotechnology, INC.; sc-166060]) followed by m-IgG Fc BP-CFL555 (1:1000 [Santa Cruz Biotechnology, INC.; sc-533654]), mouse beta-amyloid(b-4) (1:300 [Santa Cruz Biotechnology, INC.; sc-28365]), followed by goat anti-mouse IgG(H+L)AF790 (1:1000 [Invitrogen, A11375]), anti-G3BP2, (1:600 [Proteintech®, 16276-1-AP]), followed by mouse anti-rabbit IgG-CFL 680 (1:1000 [Santa Cruz Biotechnology, INC.; sc-516252]). Equal loading was ensured by SDS-PAGE followed by immunoblotting using anti-GAPDH(6C5)-AF488 (Merck, MAB374).

In addition, the same lysates were incubated final 1X Laemeli containing or not 10 % β-mercaptoethanol (BME). The samples prepared with BME were used as loading controls for the filter trap assays, while the samples prepared in non-reducing Laemmli buffer were run to assess global differences in disulfide bond formation between WT and Cse$^{-/-}$ mice. Gradient SDS–PAGE followed by Coomassie Brilliant Blue staining was performed for visualization.

LDH, PKM and pyruvate carboxylase activity assays

For all activity assays, the frozen tissues were disrupted in mild lysis buffer (25 mM HEPES, 250 mM sucrose, 20 mM $MgCl_2$, 1 mM EDTA, pH 7.4) using the TissueLyser II and 5 mm Stainless steel beads. Samples were then centrifuged at 14,000 x *g* for 15 min at 4°C, and supernatant was collected for further application. Protein concentration was performed, samples were readjusted to equal amounts and split for different activity assays. LDH (Sigma, #MAK066), PKM (Sigma, #MAK072) and pyruvate carboxylase (Abcam, #ab289840) activity assays were carried out following the manufacturer's protocol.

Direct detection of cysteine PTMs of synapsin 1 by LC-MS/MS

Brain tissues were lysed using the same protocol as for immunoblotting. A modified in-gel digestion protocol from was used to identify synapsin 1 cysteine peptides.[105] An

equal amount of protein was loaded and separated by SDS page. Gels were then stained for 2 min with a Coomassie Brilliant Blue solution (1.2 mM Coomassie Brillant Blue, 10 % acetic acid, 40 % methanol in distilled water) and destained overnight in a decoloration solution (25 % Methanol, 8 % acetic acid in distilled water). Once destained, the band corresponding to the size of the protein of interest (-/+ 5kDa) was excised. Coomassie Brilliant Blue was removed by alternating washes with 50 mM ABC and 25 mM ABC, 50 % ACN each for 10 min at 37 °C, 450 rpm. Once free from the stain, gel pieces were dried using a speed vacuum concentrator. Gel pieces were then incubated for 10 min at 4 °C with 50 mM ABC, 1 mM CaCl2, and trypsin at 12.5 ng/µl. The excess solution was removed, and samples were trypsinized for 16 h at 37 °C, 750 rpm. The following day, peptides were extracted by incubating the gel pieces two times in 0.1 % TFA for 15 min at 37°C, 450 rpm. This step was followed by two-times incubation with 0.1 % TFA + 60 % ACN for 15 min at 37°C, 450 rpm. Extracts were combined, and peptides evaporated to dryness.

Peptides were dissolved in 0.1 % TFA, and Digestion was controlled using previously described method. Peptides were analyzed using a Dionex UltiMate 3000 RSLC Systems (RSLC) system (Thermo Fisher Scientific) coupled to a timsTOF Pro (Bruker) equipped with a CaptiveSpray source. Peptide separation was carried out with an Acclaim™ PepMap™ 100 C18 column (Thermo Fisher Scientific) using a 120 min linear gradient from 3 to 35 % of B (84 % Acetonitrile, 0.1 % Formic Acid) at a flow rate of 250 nL/min. The timsTOF Pro (Bruker) was operated as previously described.

Data were evaluated with PEAKS ONLINE software using 20 ppm for precursor mass tolerance, 0.5 Da for fragment mass tolerance, specific tryptic digest, and a maximum of 3 missed cleavages. The entire mouse database was used for the search. SO-IAM (+73.020464 Da), SS-IAM (+89.086464 Da), 'Cysteine oxidation to cysteic acid' (-SO_3H, +47.984745 Da, Unimod ID: 345), carbamidomethylation (+57.021464 Da) on C, N-term acetylation (+42.010565 Da), and methionine oxidation (+15.994915 Da) were added as variable modifications, PSM and proteins were filtered at FDR 1 %. Data were normalized based on TIC.

Persulfidated G3BP2 immuno-pulldown and detection by LC/MS

90 % confluency WT and *Cse*$^{-/-}$ MEFs 10 mm dish were treated or not with 500 µM $NaAsO_2$ for the indicated times. For recovery, cells were collected 1h after the media was changed and cells removed from $NaAsO_2$. Samples lysed in HEN supplemented with 5 mM NBF-Cl. After 2 h incubation at 37 °C, proteins were precipitated using Methanol/chloroform. Samples were then redissolved in 2% SDS and incubated with 100 µM Daz-2 for 1.5 h at 37 °C before precipitation. Samples were redissolved in PBS 0.1 % SDS. An equal amount of proteins were incubated for 1 h with 1 ug of G3BP2 antibody. The SureBeads™ Magnetic Beads attached to protein A were added to the samples and incubated at 4 °C overnight. Samples were incubated for one more hour at RT, and beads were washed 3 times with PBS 0.01 % Tween and 4 times with PBS. The beads containing the G3BP2 pulldown were then resuspended in 50 mM ABC and 0.0125 µg/µl trypsin. Samples were trypsinized for 16 h at 37 °C. Supernatants were then collected, and peptides were desalted and dried as previously described. Peptides were dissolved in 0.1 % TFA, and digestion quality control was performed as previously described.

Peptides were analyzed by high-resolution LC-MS/MS using an Ultimate 3000 Nano Ultra High-Pressure Chromatography (UPLC) system (Thermo Fisher Scientific) coupled with an Orbitrap Eclipse™ Tribrid™ Mass Spectrometer via an EASY-spray (Thermo Fisher Scientific). Peptide separation was carried out with an Acclaim™

PepMap™ 100 C18 column (Thermo Fisher Scientific) using a 65 min linear gradient from 3 to 35 % of B (84 % Acetonitrile, 0.1 % Formic Acid) at a flow rate of 250 nL/min. The Orbitrap Eclipse™ was operated in a DDA mode, and MS1 survey scans were acquired from m/z 300 to 1,500 at a resolution of 120,000 using the Orbitrap mode. MS2 scans were carried out for 3 seconds with high-energy collision-induced dissociation (HCD) at 32 % using the Normal speed IonTrap mode.

Data were evaluated with PEAKS ONLINE software using 15 ppm for precursor mass tolerance, 0.05 Da for fragment mass tolerance, specific tryptic digest, and a maximum of 3 missed cleavages. The entire mouse database was used for the search. Pure S-Daz-2 (+193.0851266 Da), SO-NBF (+178.9967), NBF (+163.001791) on C, K and R, N-terminal acetylation (+42.010565 Da), and methionine oxidation (+15.994915 Da) were added as variable modifications, PSM, and proteins were filtered at FDR 1 %. Data was normalized based on TIC.

Sulfenylated G3BP2 immuno-pulldown and detection by LC/MS

90 % confluency WT and *Cse*$^{-/-}$ MEFs 10 mm dish were treated or not with 500 µM $NaAsO_2$ for the indicated times. Samples lysed in HEN supplemented with 0.5 mM of BTD. After 2 h incubation at 37 °C, proteins were precipitated using Methanol/chloroform. Immuno-pulldown processing for LC-MS and LC-MS measurments were carried out the using the protocol described above for the detection of persulfidated G3BP2.

Data were evaluated with PEAKS ONLINE software using 15 ppm for precursor mass tolerance, 0.05 Da for fragment mass tolerance, specific tryptic digest, and a maximum of 3 missed cleavages. The entire mouse database was used for the search. Pure BTD (+245.045 Da), N-term acetylation (+42.010565 Da), and methionine oxidation (+15.994915 Da) were added as variable modifications, PSM, and proteins were filtered at FDR 1 %. Data were normalized based on TIC.

G3BP2 site occupancy in 10 weeks-old WT mice brain

10-weeks old wild-type mice brain lysate from persulfidation or sulfenylation enrichment that have been already labelled with DCP-bio1 (for PSSH) and Biotin-UV-cleavable probe (for PSOH) were readjusted to the same amount. For each replicate, readjusted lysates were separate in equal amount. One part was kept for whole lysate measurement; the other part was incubated neutravidin beads for 2 h at room temperature. After incubation, samples were placed into a Micro-Spin Columns (Thermo Fisher, 89879) and span down at 500 x g for 1 min. Flow-through was collected and beads were washed two time with 2 volumes of resin with PBS 0.1% SDS. Flow-through and washes were combined forming the flow-through fraction. Both, whole lysate and flow-through were trypsinized as previously mentioned and labelled with TMT 6plex (Thermo Fisher) following manufacturer protocol. Whole lysate and flow-through of all replicates were labelled with different TMT channels and multiplexed. The multiplexed sample was then cleaned from SDS and TMT using Detergent Removal Spin Columns (Thermo Fisher, 87777) followed by desalting step as previously described. Finally, the sample was fractionated using the Pierce™ High pH Reversed-Phase Peptide Fractionation Kit.

Peptides were analyzed by high-resolution LC-MS/MS using an Ultimate 3000 Nano Ultra High-Pressure Chromatography (UPLC) system (Thermo Fisher Scientific) coupled with an Orbitrap Eclipse™ Tribrid™ Mass Spectrometer via an EASY-spray (Thermo Fisher Scientific). Peptide separation was carried out with an Acclaim™ PepMap™ 100 C18 column using a 90 min linear gradient from 3 to 35 % of B (84 %

Acetonitrile, 0.1 % Formic Acid) at a flow rate of 250 nL/min. The Orbitrap Eclipse™ was operated in a DDA mode, and MS1 survey scans were acquired from m/z 300 to 1,500 at a resolution of 120,000 using the Orbitrap mode. MS2 scans were carried out for 3 seconds with high-energy collision-induced dissociation (HCD) at 32 % using the Orbitrap mode with a resolution of 50,000.

Raw files were analyzed using Fragpipe with the TMT10 workflow parameters. 20 ppm for precursor mass tolerance and fragment mass tolerance were used. For persulfidation, NBF (+163.0096 Da) on CKR was added as variable modification. For sulfenylation, the default workflow parameters were used for the search. PSM and proteins were filtered at FDR 1 %.

EGFP-synapsin 1 in-vitro phase separation

The recombinant full-length EGFP-Synapsin 1 was expressed in a mammalian expression system and purified as previously described.[91,106] Before the experiment, EGFP-synapsin 1 was cleaned up from TCEP using a dialysis column, and the buffer was replaced with the phase separation buffer (25 mM Tris, 150 mM NaCl, pH 7.4). Hyperoxidized (PSO_xH) EGFP-synapsin 1 form was obtained by treating the protein with 100 µM DTT and 200 µM H_2O_2 at 37 °C for 30 min. Ellman's-based thiol quantification confirmed full cysteine oxidation.[107] Persulfidated EGFP-synapsin 1 was formed by treating the protein with 100 µM H_2O_2 and 500 µM H_2S for 5 min at 37 °C before adding PEG. Respective controls were carried out using the same DTT, H_2O_2, and H_2S concentrations. For the FRAP experiment, 3% w/v polyethylene glycol (PEG 3,000) was used to trigger phase separation of 10 µM EGFP-synapsin 1. Photobleaching was performed after 5 min incubation with PEG, and recovery was recorded for 10 min. 2-3 independent preparations, done on separate days and with separate protein batches, were used per thiol modifications.

To further confirm that cysteine modifications were responsible for the observed effect, we used GFP–synapsin 1 in which all cysteines had been pre-blocked with 300 µM IAM for 20 minutes at 37 °C and repeated the DTT + H_2O_2 and H_2O_2 + H_2S treatments as previously described.

Synapsin 1 PSOH and PSSH formation were verified by monitoring in-gel fluorescence of modified protein after chemoselective labeling with BTD coupled to Cy5[108] and Daz-2 coupled to Cy5[4] respectively.

Primary neurons experiments

Primary hippocampal neurons were prepared from newborn pups (p0/p1) and the exocytosis assays were performed as described recently.[6] Neurons were pre-incubated with GYY4137 (100 µM) or propargylglycine (1 mM) and aminooxiacetic acid (1 mM). During imaging, neurons were first perfused with Tyrode solution supplemented with 2.5 mM KCl (low KCl); subsequently, to stimulate exocytosis, neurons were perfused with Tyrode solution supplemented with 92.5 mM KCl (high KCl) for 5 min; finally, neurons were briefly perfused with Tyrode solution containing 50 mM NH4Cl to alkalize the sample and visualize the total fluorescence from synaptophysin-pHlurin.

G3BP2 in-vitro phase separation

Total RNA from STHdhQ7/Q7 cells was extracted using the RNeasy Midi Kit and following the manufacturer's protocol. Total RNA was resuspended in RNase-free water, and concentration was assessed using a Nanodrop.

G3BP2 was purchased from Biomol (#349926). First, isolated G3BP2 was

labeled with a Cyanine3 NHS ester probe. The protein buffer was briefly exchanged with the labeling buffer (100 mM Sodium Bicarbonate, 50 mM NaCl, pH 8.0) using the Micro Bio- Spin™ 6 Columns following the manufacturer's protocol. The protein was then incubated for 1 h at RT with Cyanine 3 NHS ester probe at a ratio of 1:3 (protein: Cyanine3). After incubation, the probe excess was removed using the Micro Bio-Spin™ 6 Columns and the buffer was exchanged with phase separation buffer. To minimize the effect of the Cy3- label on phase separation, the labeled proteins were mixed with non-labeled G3BP2 at a 1:9 ratio (labeled: non-labeled). For hyperoxidized (PSO_xH) G3BP2, 10 µM of the protein was incubated in the presence of 100 µM DTT and 200 µM H_2O_2 for 30 min at 37°C. Ellman's-based thiol quantification confirmed full cysteine oxidation.[107] The reduced (PSH) and oxidized (PSOH/PSSP) G3BP2 were generated using the same concentration of respectively DTT or H_2O_2. To further confirm that cysteine modifications were responsible for the observed effect, we used Cy3-G3BP2 in which its cysteine had been pre-blocked with 300 µM IAM for 20 minutes at 37 °C and repeated the DTT or H_2O_2 treatments as previously described.

For all experiments, G3BP2 phase separation was triggered with 50 ng/µl of total RNA extract and incubated 7 min prior to FRAP experiments. Recovery was recorded for 10 min.

Persulfidation-driven dissolution of G3BP2 droplets

20 µM of non-labelled G3BP2 were incubated with 40 µM of DTNB and 50 ng/µl of RNA for 10 min prior addition of 50 µM of H_2S. Upon H_2S addition, recording was started and dissolution was acquired for 20 mins. In a separate experiment, the yield of PSSH was estimated by monitoring the TNB absorbance at 412 nm, following H2S addition. ~95 % yield was obtained, in agreement with our previous report using same protocol.[50,66] The dissolution experiment was performed in 3 separate reconstitutions. Images were acquired using an Evident CSU-W1 spinning disk confocal microscope equipped with a Teledyne Prime BSI sCMOS camera with a 60× Silicone objective lens.

G3BP2 WT and C73S mutant plasmid construction

The pDEST-CMV-N-EGFP-wtG3BP2 plasmid was built using the gateway cloning method.[109] The human G3BP2 sequence from the pENTR4_G3BP2 plasmid was transferred into the pDEST-CMV-N-EGFP plasmid using the Gateway™ LR Clonase™ following the manufacturer's instructions. Both plasmids were obtained through Addgene. pENTR4_G3BP2 was a gift from Thomas Tuschl (Addgene plasmid #127105; http://n2t.net/addgene:127105; RRID:Addgene_127105). pDEST-CMV-N-EGFP was a gift from Robin Ketteler (Addgene plasmid # 122842; http://n2t.net/addgene:122842; RRID:Addgene_122842).

For the C73S mutation, the point mutation was created following established protocol.[109] Plasmids were first tested for the mutation using PCR primers allowing the elongation of a smaller fragment when the mutation is present (FW: GACTTCAAGGAGGACGG; RV: GTCTCAGCGACGCTG; RV middle primer: ACATGACGAATTTTAGTATGACT). Positive clones were then sent for sequencing for further validation. Both pDEST-CMV-N-EGFP-wtG3BP2 and pDEST-CMV-N-EGFP- C73SG3BP2 plasmids were amplified and extracted using PureLink™ HiPure Plasmid Maxiprep Kit (Invitrogen™, K210007) before use.

Plasmid transfection and G3BP2 live cell microscopy

Cse$^{-/-}$ and WT MEF cells were transfected with pDEST-CMV-N-EGFP-C73SG3BP2 or

pDEST- CMV-N-EGFP-wtG3BP2 using a reverse transfection protocol. Briefly, the transfection solution was prepared by mixing 1 part of plasmid DNA (in µg) and 3 parts of TransIT®- 2020 Transfection Reagent (Mirius, #MIR5400) in Opti-MEM™ I Reduced Serum Medium (Gibco™, #31985062) and incubated for 30 min. Meanwhile, cells were trypsinized for 3 min, followed by quenching with DMEM supplemented with 10 % fetal bovine serum. After incubation, the transfection solution was added into a glass bottom µ-slide with 8 wells at 50 ng of DNA per well (IBIDI, #80807). 15,000 cells were seeded in each well on top of the transfection reagent and incubated for 24 h. The day after, the media was changed 2 h before starting the experiment to allow cell recovery from transfection stress.

Live cell microscopy was carried out using a Leica SP8 LIGHTNING or Nikon AX R NSPARC laser scanning confocal microscope with a 63x water or oil objective respectively. Environmental control (37 °C, 5 % CO_2) and adaptive focus control were used.

G3BP2 live cell microscopy

For the measurements of stress granule formation, cells were treated with 5 µg/mL Hoechst 33342 for 5 min. Media containing Hoechst 33342 was washed 2 times and replaced with FluoroBrite™ DMEM supplemented with 2 mM L-glutamine, 1 % penicillin-streptomycin and 10 % fetal bovine serum. Cells (MEF WT or *Cse*$^{-/-}$) transformed with WT G3BP2 or (mutant) C73S-G3BP2 were treated with 500 µM sodium metaarsenite ($NaAsO_2$), and one image was taken every 16 sec for 20 min. The number and size of stress granules were quantified using Fiji.

Live H_2S treatment

For the in-cellulo H2S dissolution of G3BP2 condensates, WT MEF cells were treated for 15 min with 500 µM $NaAsO_2$ to allow the formation of G3BP2 condensates. Cells were then recorded every 16 sec, and Na_2S was injected at a 100 µM final concentration. After the condensate reformed, a second injection of H_2S at the same concentration was performed. The number and size of stress granules were quantified using Fiji.

In-cellulo FRAP

WT and *Cse*$^{-/-}$ MEFs were treated with 500 µM $NaAsO_2$ as previously described. After 15 min, the photobleatching was induced using 4 pulses at 100 % laser power, and recovery was imaging every 3 seconds. FRAP analysis was performed using Fiji.

Immunofluorescence of G3BP2 under $NaAsO_2$ treatment

MEF, STHdh cells or human fibroblast were split in a µ-Dish 35 mm, high Glass Bottom (IBIDI, #81158). For all experiments, cells were treated with 500 µM of sodium(meta)arsenite ($NaAsO_2$). GYY4737 was used at 200 µM during the one hour recovery. For ergothioneine (ET) experiments, WT or *Cse*$^{-/-}$ MEFs were pre-treated with 400 µM ergothioneine for 2h before treatment with 500 µM $NaAsO_2$. ET was omitted during stress induction to prevent cross reaction with arsenite. The media was then supplemented again with ET during recovery.

Fixation and immunofluorescence

Before fixation, cells were washed two times with warm PBS and fixed with 2 % PFA for 10 min, followed by 10 min with 4 % PFA. Cells were washed from PFA with 3 times cold PBS. For immunofluorescence, the permeabilization step was performed in

PBS 0.1 % TritonX100 for 20 min. Cells were then incubated for 1 h in blocking buffer (1 % BSA, 22.52 mg/ml glycine, 0.1 % Tween in PBS) followed by a 2 h incubation at 37 °C with anti-G3BP2, (1:600 [Proteintech®, 16276-1-AP]) Cells were washed and incubated with secondary antibody (mouse anti-rabbit IgG-CFL 647, [Santa Cruz Biotechnology, INC.; sc-516251]) for 2 h at 37 °C. After washing the cells, DAPI (4',6-Diamidin-2-phenylindol, Dihydrochloride; Thermo Fisher Scientific) staining was performed prior to recording, following the manufacturer protocol.

Recording

Imaging was performed using either Leica SP8 LIGHTNING Confocal Microscope with a 63x oil objective and a resolution of 2048 x 2048 or using an Evident CSU-W1 spinning disk confocal microscope equipped with a Teledyne Prime BSI sCMOS camera with a 100 × 1.45NA oil UPLXAPO100XO objective lens.

Immunofluorescence for the co-localisation of stress granule proteins

MEFs seeded into 8-well^{high} Glass Bottom µ-slides (IBIDI, 80807) were treated with $NaAsO_2$ for indicated time periods, followed by washes and fixation, permeabilization and blocking as already described. Samples were incubated with anti-G3BP2, (1:600 [Proteintech®, 16276-1-AP]) for 2 h incubation at 37 °C, followed by washes and incubation with secondary antibody ((mouse anti-rabbit IgG-CFL 488 [Santa Cruz Biotechnology, INC.; sc-516248]), mouse anti-TDP43-AF790 (1:250 [Santa Cruz Biotechnology, INC.; sc-376311]), mouse anti-eIF4G-AF594 (1:250 [Santa Cruz Biotechnology, INC.; sc-133155]), and mouse anti-TIA-1/TIAR(D-9)AF-647 (1:250 [Santa Cruz Biotechnology, INC.; sc-48371]) for 2 h at 37 °C. DAPI (4',6- Diamidin-2-phenylindol, Dihydrochloride; Thermo Fisher Scientific) staining was performed prior to recording, following the manufacturer's protocol. Images were acquired on a Leica Stellaris confocal microscope with White Light Laser, using a HC PL APO CS2 100x/1.40 oil objective lens and a resolution of 1024 x 1024.

Image analysis

All images were converted to TIF using Fiji software. TIFs where then analyzed using an in-house built python script. For datasets containing Z stacks, average intensity projection was used to produce a Z-projected image used for further analysis. Cell segmentation was performed using Cellpose deep-learning framework (cyto3 model). To improve segmentation, we use a composite image of DAPI signal and proteins spread in the cytoplasm. Before segmentation, images were downscale to 256x256 in resolution to match Cellpose requirements. The resulting masks were then upscaled to the original resolution using the nearest-neighbour interpolation, producing per-cell masks used throughout the quantification pipeline.

The granule detection was performed independently for each protein if applicable, using an automated multistep procedure that includes: (1) White top hat filter (disk radius = 5px); (2) Global thresholding using Otsu threshold method, weighted by a constant factor to supress weak background puncta; (3) Particle analysis on the binary mask using a morphological size filtering followed by connected-component labelling (scikit-image). This approach ensured robust granule detection across different intensities and imaging conditions without manual parameter tuning.

To determine the number and size of granules per cells, overlapping granules with the segmented cells were measured and 3 metrics were computed, the granule counts, the total granule area, and the granule density per cell (total granule area / cell area).

For the granule colocalization analysis, cell segmentation and thresholding

were performed as described above. A condensate restricted colocalization analysis was performed to avoid misleading whole cell corelation. All colocalization metrics were computed only within granule pixels for each pair of proteins. For each segmented cell and pair of proteins an object based Mander's coefficient was calculated, quantifying the proportion of granule spatially co-occurring, independently from the pixel intensity.

Western blot detection of global and G3BP2 PSSH and PSOH levels under $NaAsO_2$ treatment

WT MEFs were treated or not with 500 µM of $NaAsO_2$ for the indicated time. Cells were lysed in HEN buffer supplemented either with 5 mM NBF-Cl for persulfidation or 0.5 mM BTD for sulfenylation. Sample preparation and enrichment step for both modifications were performed as previously described except for the elution step. Briefly, after incubation and washing steps, the Pierce™ High Capacity NeutrAvidin Agarose beads were resuspended in 50 mM Hepes, 1X Laemmli and boiled at 95 °C for 10 min to release enriched proteins. Part of the sample before enrichment was taken to be used as a loading control. Both Loading control and enriched fraction were then run on a 10% acrylamide gel and transferred to a nitrocellulose membrane. The streptavidin, Dylight™ 633 conjugated was used to detect the global persulfidation and sulfenylation levels. Anti-G3BP2 antibody (1:4000) and secondary anti-rabbit IgG H&L Alexa Fluor® 680 (1:20,000) and anti-GAPDH-AF488 (Sigma-Aldrich, MAB374-AF488, 1:2000) were used for immunoblotting.

Thermal proteome profiling MEF WT and *Cse*$^{-/-}$ under H_2O_2 treatment

WT and *Cse*$^{-/-}$ MEFs were trypsinized and washed 3 times in cold serum-free DMEM. After the last centrifugation, cells were resuspended in 1.2 ml of DMEM supplemented with 10 % FCS and treated for 60 min with 500 µM H_2O_2 on ice. After 60 min, an equal number of cells were aliquoted into different tubes and gently centrifuged. Cell pellets were resuspended in 20 µl serum-free media and heated at 25, 47, or 57 °C for 3 min. Cells were brought back to room temperature for 3 min and lysed with freeze- thaw cycles. Extracted proteins were subjected to ultracentrifugation at 100,000 x g for 20 min at 4 °C. The volume corresponding to 50 µg in the 25 °C-exposed cells was used for all samples. Proteins were subsequently denatured using 3M Gu-HCl for reduction and alkylation steps with 500 µM DTT and 5 mM IAM for 30 min at 37 °C, respectively and then subjected to tryptic-digestion. Peptides were desalted as previously described. Eluates were evaporated to dry and resuspended in 100 mM triethylammonium bicarbonate for TMT labeling. Samples were labeled using the TMTpro™ 16plex Label Reagent Set. Samples were combined, desalted, and dried as previously described and subjected to LC/MS analysis by Orbitrap Eclipse™ Tribrid™ Mass Spectrometer via an EASY-spray (Thermo Fisher Scientific).

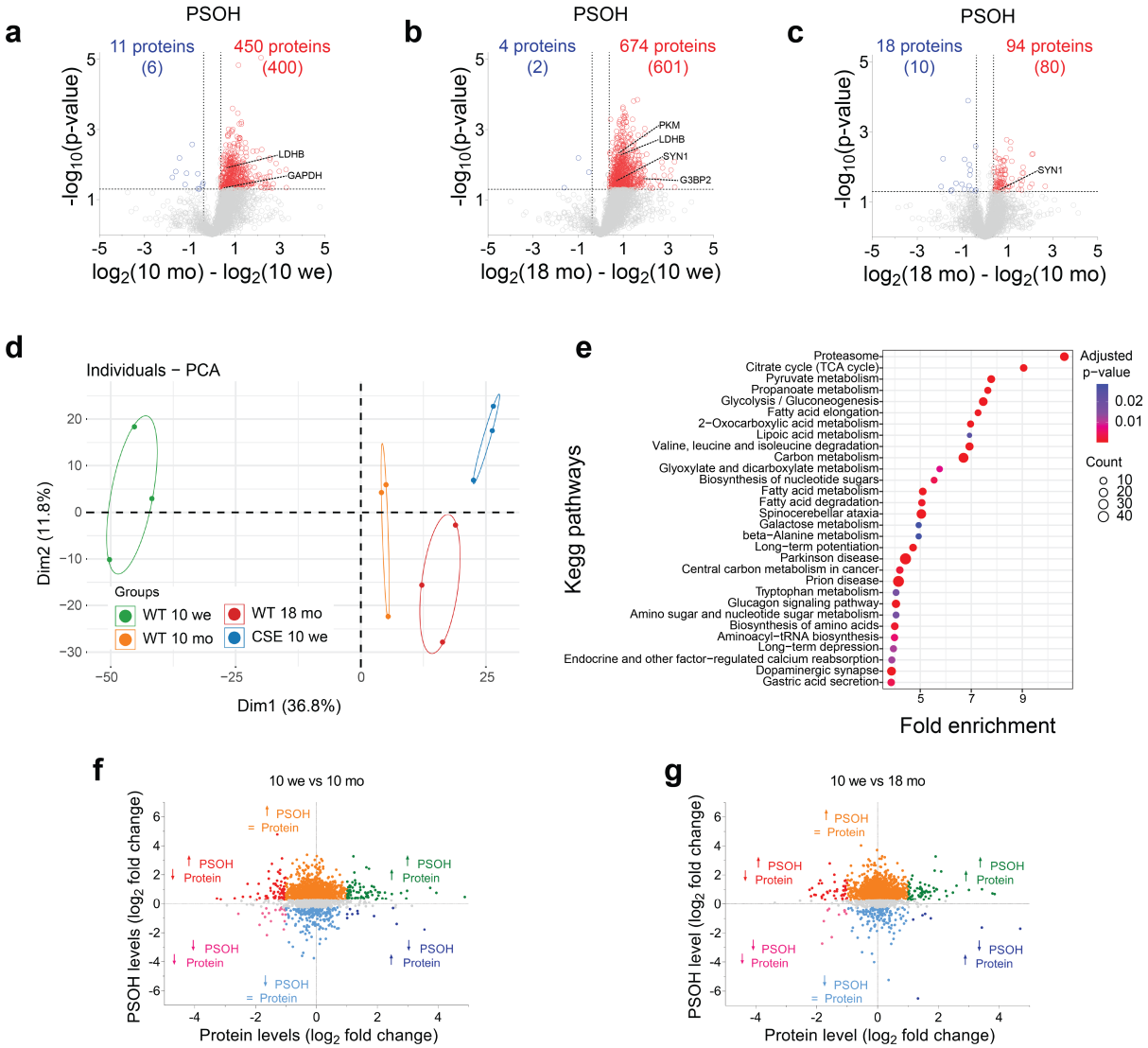
Data were evaluated using FragPipe software [110] using 10 ppm for precursor mass tolerance, 0.02 Da for fragment mass tolerance, specific tryptic digest, and a maximum of 3 missed cleavages. Carbamidomethylation (+57.021464 Da), N-term acetylation (+42.010565 Da), and methionine oxidation (+15.994915 Da) were added as variable modifications. TMTpro (+304.207146 Da) was added as fixed modification on K and peptide N-term, peptide-spectrum match (PSM), and proteins were filtered at FDR 1 %. TMT quantification was performed at the MS2 level.

Brain Section and Gallya's staining

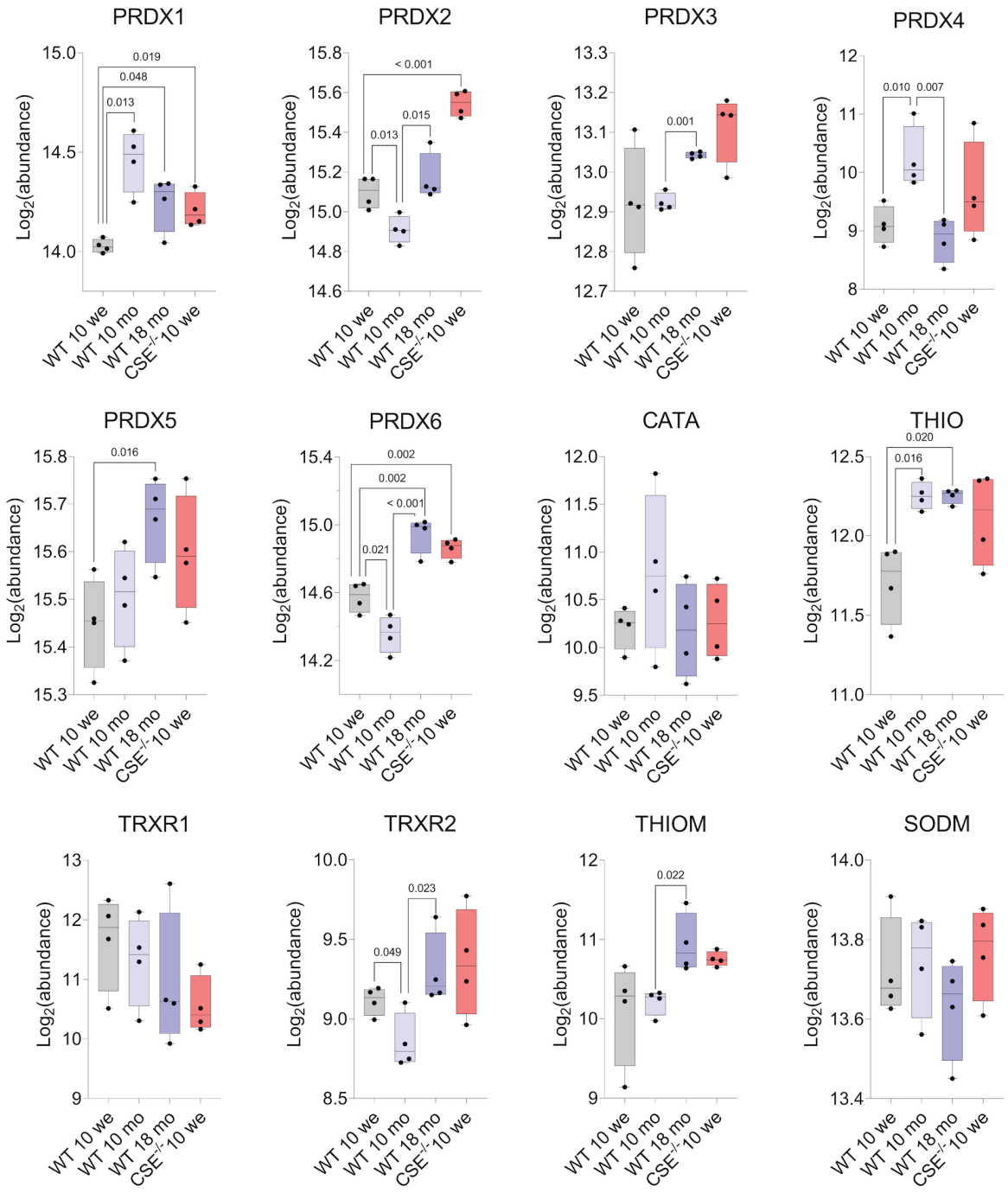
Brains were extracted and fixed in 4 % paraformaldehyde solution for 24 h at 4 °C,

dehydrated in ethanol (30–100 %), and enlightened in xylene. After embedding in Histowax® (Histolab Product AB, Göteborg, Sweden), tissue blocs were sectioned to 5 µm thickness on a rotary microtome (RM 2125RT Leica Microsystems, Wetzlar, Germany). Gallya's silver staining was performed following the manufacturer’s protocol (Morphisto, Offenbach am Main, Germany).

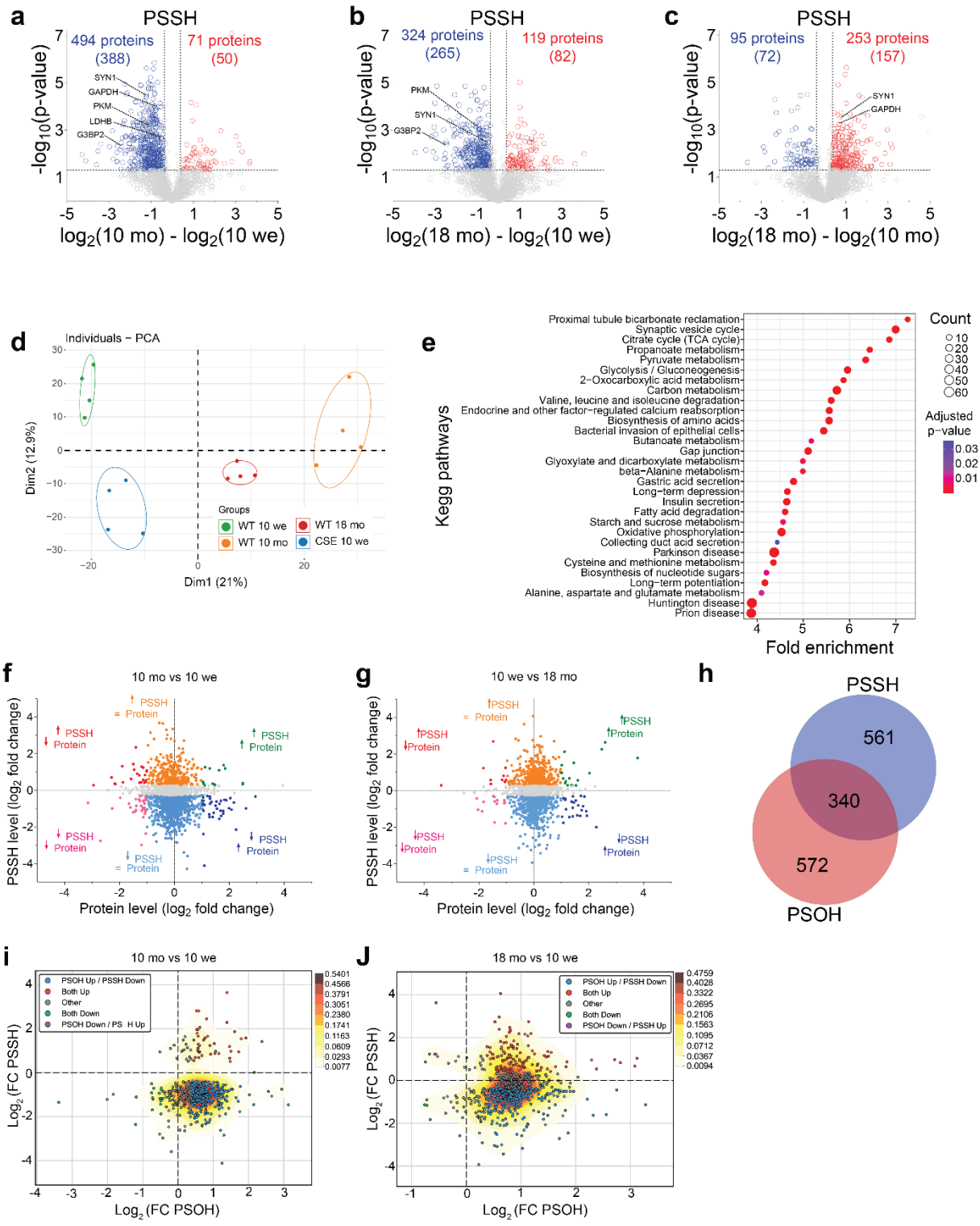
Extended data figures



Extended data Fig. 1. Quantitative sulfenylomics analysis of aging brain. (**a-c**) Volcano plot analysis of PSOH changes in (**a**) 10-month-old mice and (**b**) 18-month-old mice relative to 10-week-old mice and (**c**) 18-month-old mice relative to 10-month-old mice (n = 3, Welch's t-test). The number of proteins with significantly altered PSOH levels is indicated, with the number in parentheses reflecting proteins identified through a minimum of 2 unique peptides. (**d**) Principal component analysis (PCA) underscoring the reproducibility of sulfenylome measurements across all replicates. (**e**) KEGG pathway enrichment analysis of proteins showing significant PSOH changes with age. The graph shows the top 30 significant (Benjamini adjusted p-value ≤ 0.05) and most enriched pathways, with the color gradient indicating adjusted p-values and circle size the number of proteins. (**f-g**) Scatter plot analysis of sulfenylome and protein expression relationships. log2 fold changes within the sulfenylome (y-axis) were plotted against total proteome changes (x-axis) for the (**f**) 10-month-old vs. 10-week-old mice and (**g**) 18-month-old vs. 10-week-old mice.

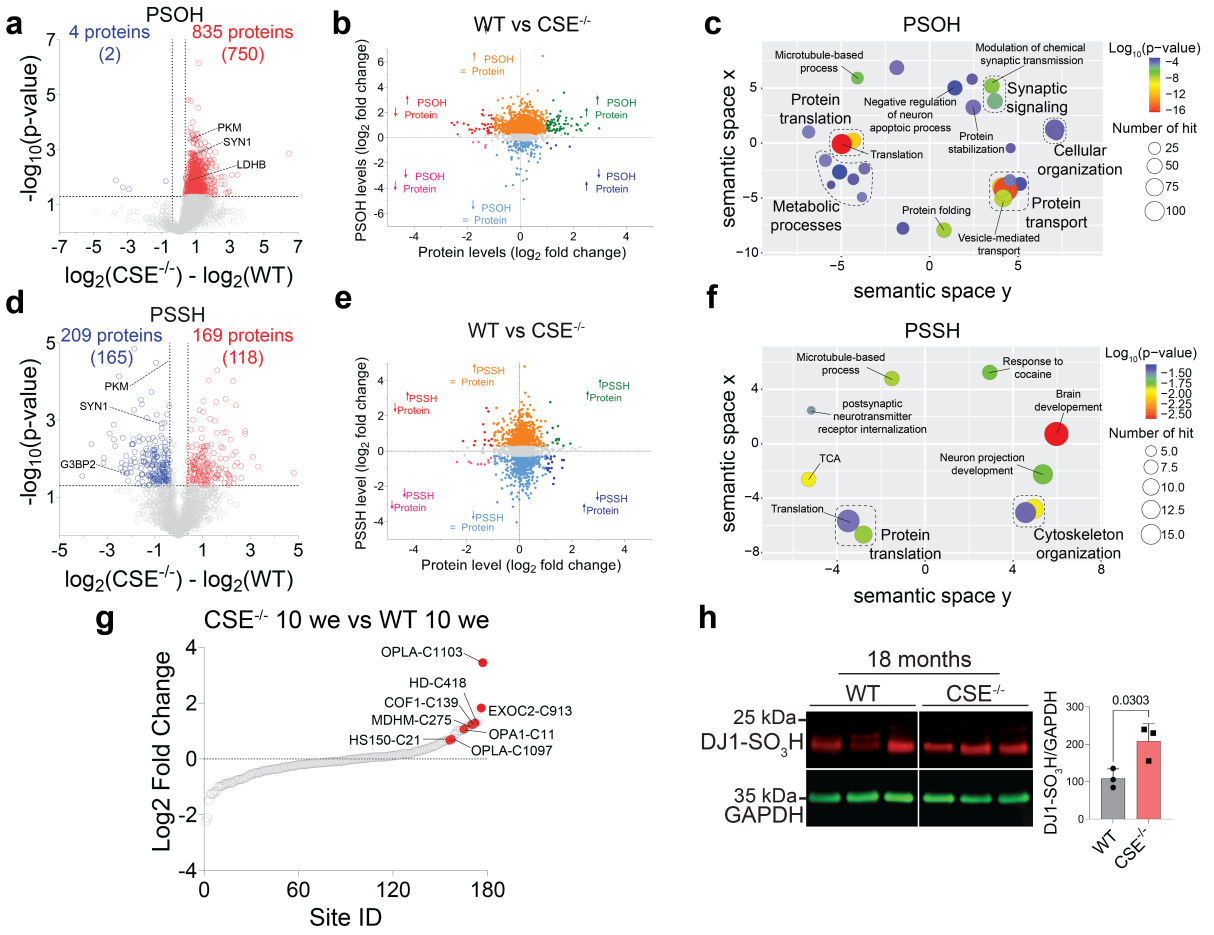


Extended data Fig. 2. Expression profiles of antioxidant proteins across aging and in *Cse*$^{-/-}$ mice. Whiskers and box plots of the log2 transformed abundancies of antioxidant proteins identified in the proteome analysis. Reported significance levels accompanying the plots are directly correlated with the p-values calculated through the proteome analysis (n = 4). PRDX (1-6): peroxiredoxin (1-6); CATA: Catalase; THIO: thioredoxin, THIOM: mitochondrial thioredoxin; TRXR (1-2): thioredoxin reductase (1-2); SODM: mitochondrial superoxide dismutase.



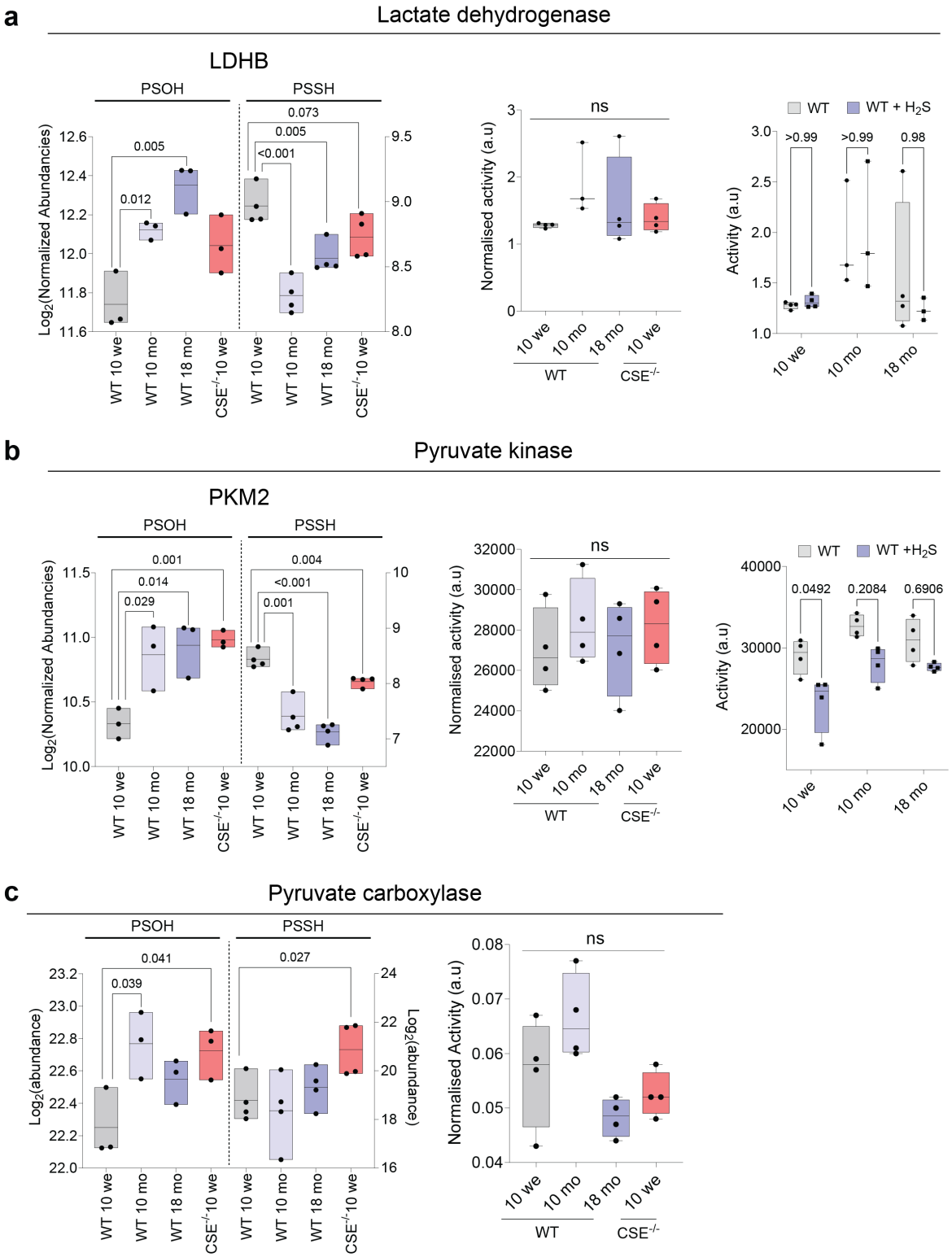
Extended data Fig. 3. Quantitative persulfidomics analysis of aging brain. (**a-c**) Volcano plot analysis of persulfidome changes in (**a**) 10-month-old mice and (**b**) 18-month-old mice relative to 10-week-old mice and (**c**) 18-month-old mice relative to 10-month-old mice (n = 4, Welch's t-test). The number of proteins with significantly altered PSSH levels is indicated, with the number in parentheses reflecting proteins identified through a minimum of 2 unique peptides. (**d**) Principal component analysis (PCA) underscoring the reproducibility of persulfidome measurements across all replicates. (**e**) KEGG pathway enrichment analysis of proteins showing significant PSSH changes with age (based of FDR adjusted p value ≤ 0.05). The graph shows the top 30 significant (Benjamini adjusted p-value ≤ 0.05) and most enriched

pathways, with the color gradient indicating adjusted p-values and circle size the number of proteins. (**f-g**) Scatter plot analysis of PSSH and protein expression relationships. log2 fold changes within the persulfidome (y-axis) were plotted against total proteome changes (x-axis) for the (**f**) 10-month-old vs. 10-week-old mice and (**g**) 18-month-old vs. 10-week-old mice. (**h**) Venn diagram comparing sulfenylated and persulfidated proteins found to significantly change with aging. (**i-j**) Log_2 fold change correlation of proteins significantly changing (Welch´s test, FDR adjusted p-value) and passing 30 % threshold in at least one of the two modifications in (**i**) WT 10 mo vs WT 10 we and (**j**) WT 18 mo vs 10 we. A two-dimensional kernel density estimate (KDE) was used to estimate and represent overall distribution of protein changes. KDE is represented by colour gradient on the scatterplot.

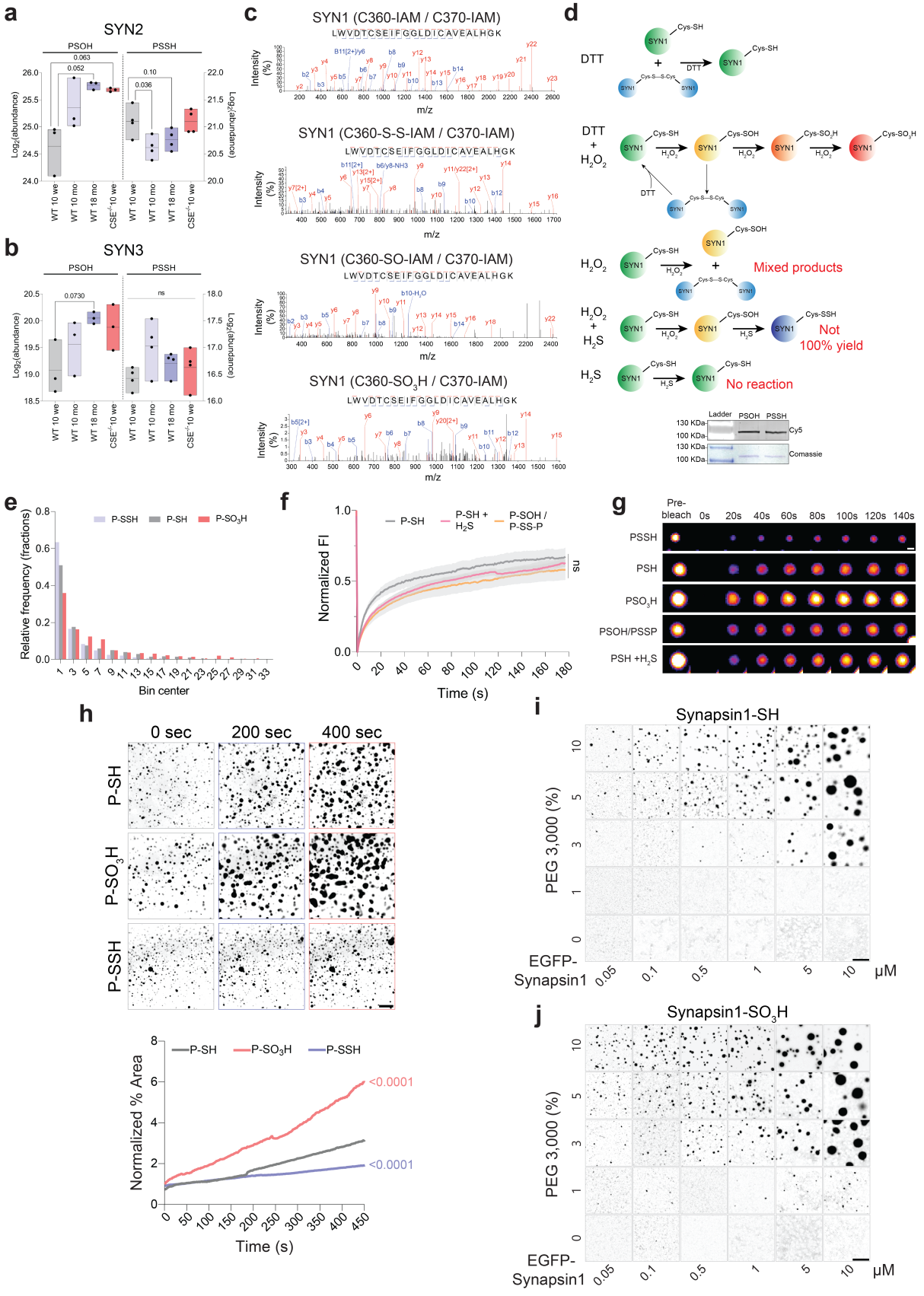


Extended data Fig. 4. The effect of CSE on persulfidation, sulfenylation and sulfonylation of proteins. (**a**) Volcano plot analysis of PSOH changes in 10-month-old *Cse*$^{-/-}$ mice vs. 10-month-old wild type mice (n = 4, Welch's t-test). (**b**) Scatter plot analysis of PSOH and protein expression relationships. log2 fold changes within the persulfidome (y-axis) were plotted against total proteome changes (x-axis) for the 10-month-old *Cse*$^{-/-}$ and wild type mice. (**c**) GO (Biological process) term enrichment analysis of proteins showing PSOH increase (Welch's t-test) in *Cse*$^{-/-}$ mice. Enrichment was performed using DAVID[22,23] and the results visualized through REVIGO.[24] Benjamini adjusted p-value ≤ 0.05. **d**) Volcano plot analysis of PSSH changes in 10-month-old *Cse*$^{-/-}$ mice vs. 10-month-old wild type mice (n = 4, Welch's t-test). **e**) Scatter plot characterizing log2 fold changes within the persulfidome (y-axis) and protein expression (x-axis) for comparison between 10-month-old *Cse*$^{-/-}$ and wild type mice. **f**)

GO (Biological process) term enrichment analysis of proteins showing significant PSSH decrease (Welch's t-test) in *Cse*$^{-/-}$ mice (Benjamini adjusted p-value ≤ 0.05). **g**) The proteome-wide and site-specific changes in protein sulfonylation in 10-wek old *Cse*$^{-/-}$ vs their wild type littermates (n = 4, Welch's t-test). **h)** DJ1 (PARK7) sulfonylation levels in 18-month-old WT and *Cse*$^{-/-}$ mice. The intensities were normalized to the GAPDH expression levels. Values represent mean ± SD (Student's t-test, n = 3). (**i-n**) Prediction of the structural changes caused by cysteine sulfonylation that is observed in *Cse*$^{-/-}$ mice. Modeling was performed using VIENNA-PTM. (**i**) Heat shock protein 105 kDa (HS105) is based on the 6GFA.pdb model.[111] (**j**) Glutamine synthetase (GLNA) is based on the 2OJW.pdb model.[112] (**k**) Fatty acid synthase (FAS) is based on 5MY2.pdb model.[113] (**l**) 5-oxoprolinase (OPLA) is based on the AF-O14841-F1-model_v4.pdb model.[114] (**m**) Membrane-associated progesterone receptor component 2 (PGRC2) based on AF-Q80UU9-F1- model_v4.pdb model.[114] (**n**) Poly(rC)-binding protein 1 (PCBP1) is based on the AF-Q15365-F1- model_v4.pdb model.[114]

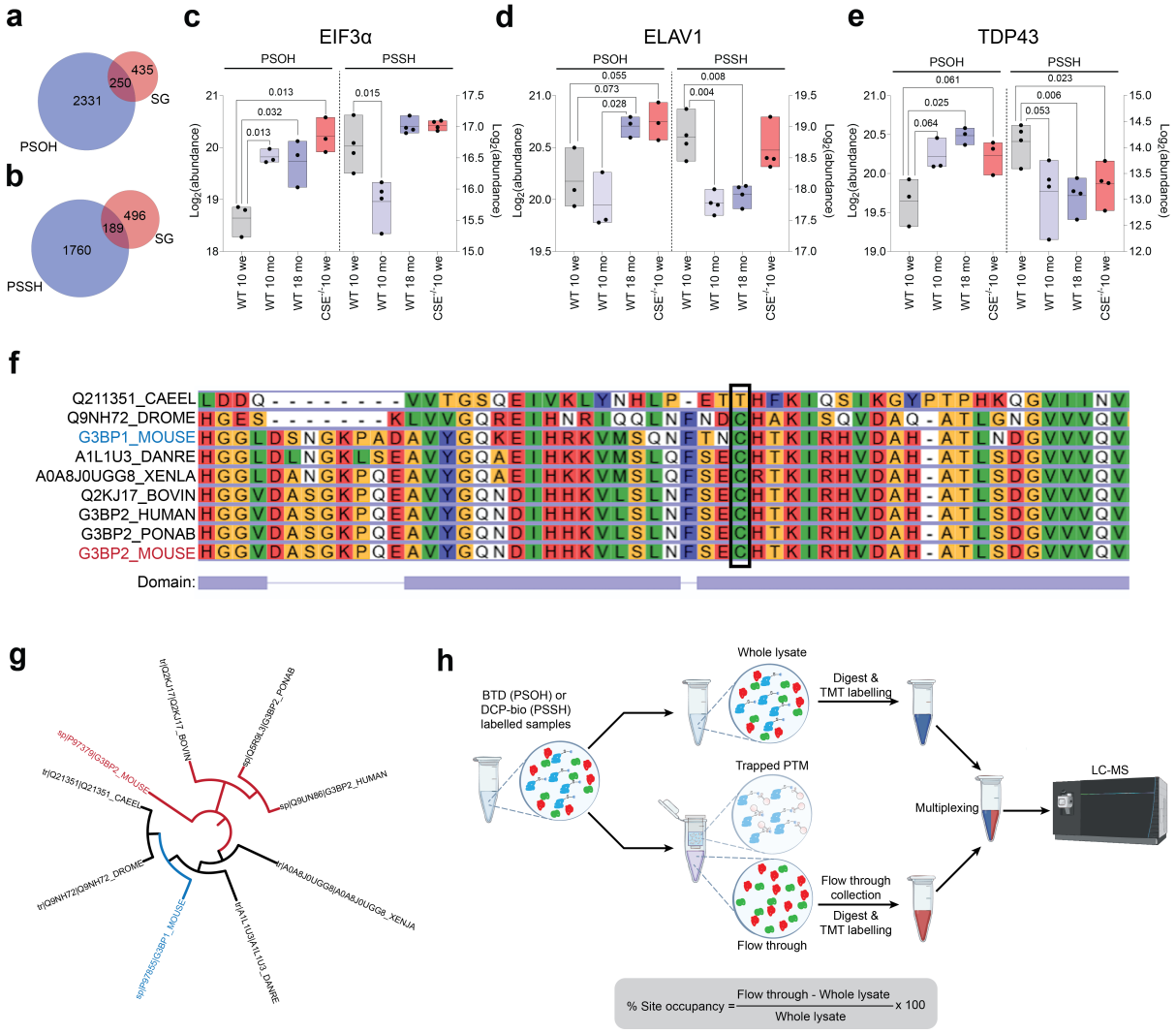


Extended data Fig. 5. Age-induced thiol remodeling predominantly affects proteins known to undergo LLPS. (**a-c**) Age-induced sulfenylation and persulfidation changes of metabolic enzymes show no impact on their activity. (**a**) Lactate dehydrogenase B (LDHB), (**b**) pyruvate kinase (PKM) and (**c**) pyruvate carboxylase, all key metabolic enzymes, show significant changes of sulfenylation and persulfidation with aging and/or *Cse*$^{-/-}$ (left, Welch's t-test) but no significant change could be observed in their activity (middle, 1-way Anova, n.s. non-significant) even after addition of 10 μM H_2S to a freshly prepared brain lysate (right, paired two-way Anova).

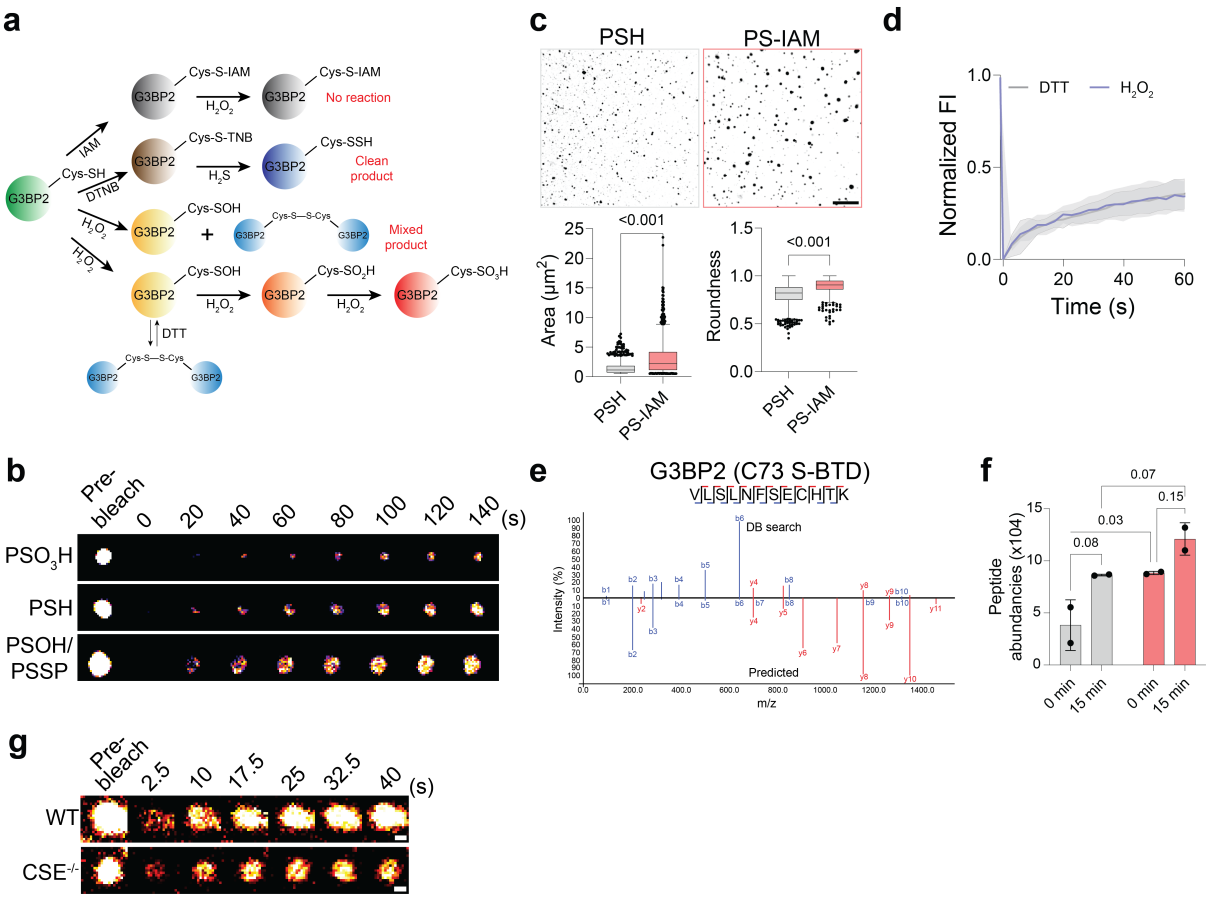


Extended data Fig. 6. Age-induced changes in synapsin's thiol oxidation affect its LLPS properties. (**a-b**) Boxplot of the PSOH and PSSH remodelling of (**a**) synapsin 2 and (**b**) synapsin 3 in aging wild-type and *Cse*$^{-/-}$ mouse brain (n ≥ 3, Welch's t-test; p-value reported

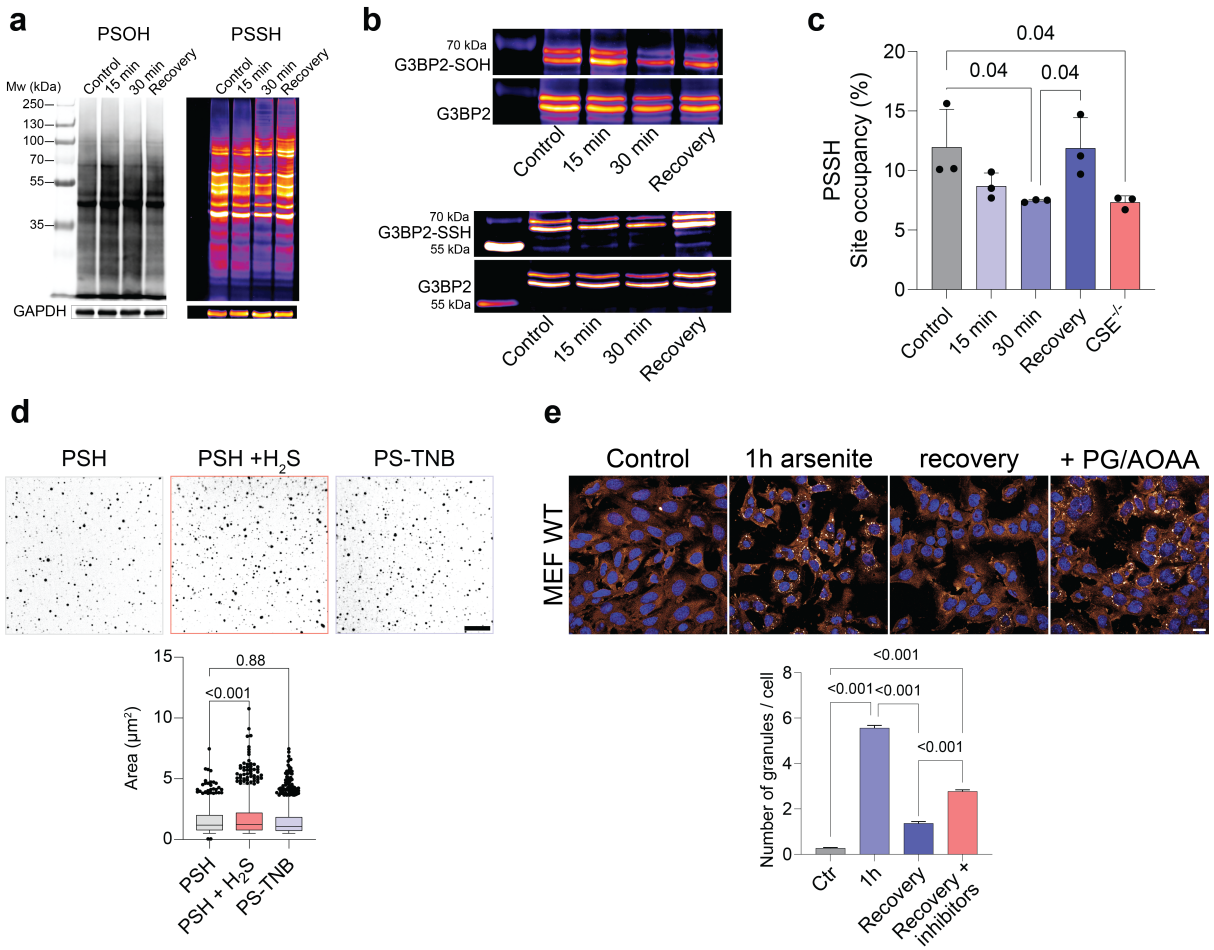
from proteomic analysis). **c**) Annotated TimsTOF CID MS/MS spectra of synapsin 1 peptides highlighting distinct oxidation states of cysteine 360. Spectra originate from quantified peptides extracted from WT and *Cse*$^{-/-}$ 18-month-old mice, as depicted in Fig. 3c. The y-ions are denoted in red, while the b-ions are indicated in blue. (**d**) Schematic representation of the protocols for preparation of different cysteine modifications, used for the phase separation and FRAP experiments. PSH (100 µM DTT), PSSH (100 µM H_2O_2 + 500 µM H_2S), PSO_3H (100 µM DTT + 200 µM H_2O_2), and PSOH/PSSP (200 µM H_2O_2). DTT reduced EFGP-synapsin 1 was also treated with 500 µM H_2S as a negative control. Inset: In-gel detection of persulfidated and sulfenylated EFGP-synapsin 1, prepared by the protocols depicted in the scheme. Daz-2 and BTD, clicked to Cy5-alkyne or azide were used to visualize PSSH and PSOH, respectively. Coomassie blue staining was used to show the protein load. (**e**) Relative frequency histogram of EFGP-synapsin 1 droplets in relation to their size. (**f**) Quantification of fluorescence recovery after photobleaching. Prior to initiating phase separation, 10 µM EFGP-synapsin 1 samples underwent treatment with various cysteine-modifying agents as depicted in (**d**). Subsequent phase separation was induced by 3% PEG3000 (n ≥ 2 replicates, N = 30-50 condensates per condition, two-way ANOVA, Sidak posthoc test, n.s. non-significant). (**g**) Representative microscopy images capturing EGFP-synapsin 1 condensates before and after photobleaching. Scale bar = 1 µm. (**h**) Wetting of EGFP-synapsin 1 condensates (n ≥ 2 replicates, N = 30-50 condensates per condition, two-way ANOVA, Sidak posthoc test). Scale bar = 20 µm. (**i-j**) Phase diagram of EGFP-synapsin 1 LLPS**.** Representative images of the LLPS phase diagram formed with (**i**) the reduced or (**j**) sulfonylated EGFP-synapsin 1. The phase diagram was built using increased concentrations of both the protein and PEG3000 concentration. Scale bar = 5 µm.



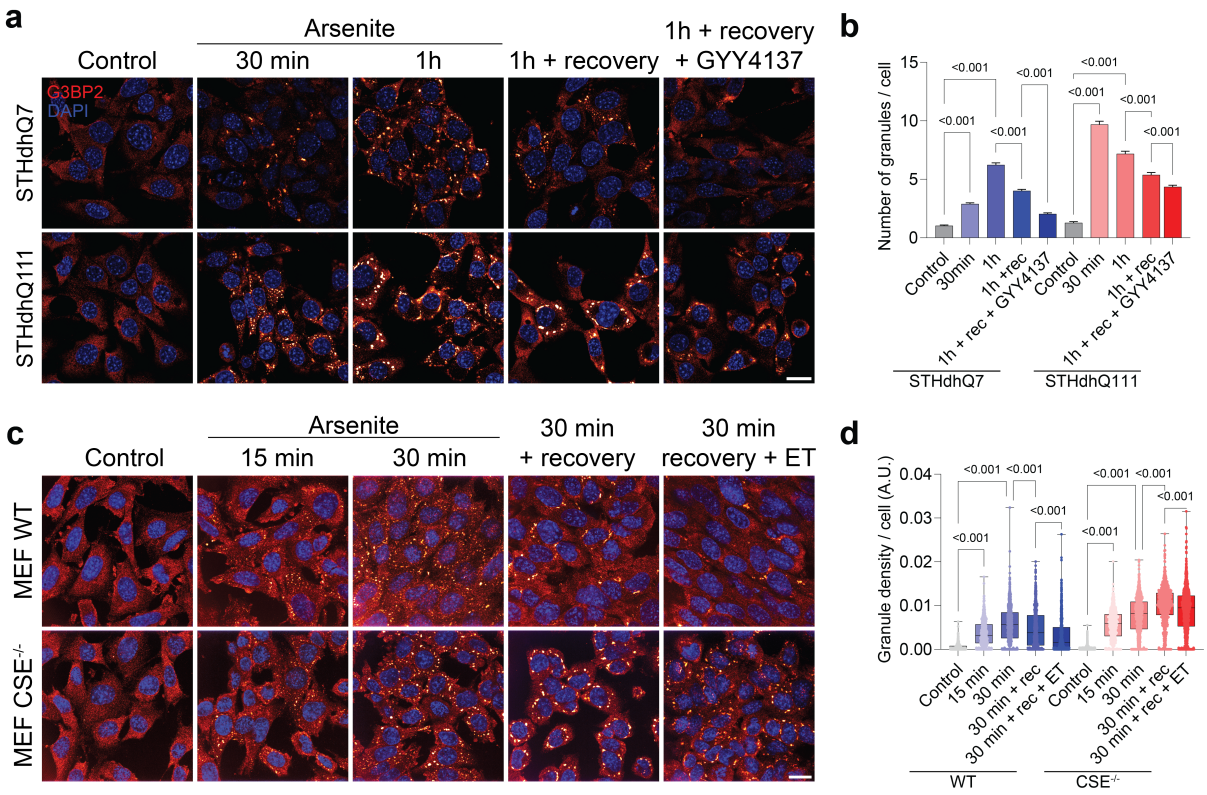
Extended Data Fig. 7. Age-induced thiol remodelling affects stress granule proteins. (**a-b**) Venn diagram representing the overlap of proteins present in stress granules (SG) and those identified in (**a**) PSOH and (**b**) PSSH data sets. (**c-e**) Boxplot of the age-induced PSOH and PSSH changes of (**c**) eIF3α, (**d**) ELAV1 and (**e**) TDP-43. (n ≥ 3, Welch's t-test; p-value reported from proteomic analysis). (**f**) Sequence alignment of G3BP2 focused of the cysteine 73 region. The conserved cysteine residue, positioned at C73 in the mouse G3BP2 sequence, is highlighted with a black rectangle. Conservation of this cysteine across species underlines its potentially important role in the protein's function, such as its phase separation potential. (**g**) Circular phylogenetic cladogram build using G3BP2 sequences alignment from a range of species: *Mus musculus* (MOUSE), *Bos taurus* (BOVIN), *Pongo abelii* (PONAB), *Homo sapiens* (Human), *Xenopus laevis* (XENA), *Danio rerio* (DANRE), Drosophila melanogaster (DROME), and *Caenorhabditis elegans* (CAEEL). For contextual comparison, G3BP1 from *Mus musculus* is also included. (**h**) Schematic representation of the sample preparation to determine PSOH and PSSH site occupancy in 10 week-old WT mice brain. Shortly, lysate labelled for either PSOH (BTD – UV-cleavable probe) or PSSH (DCP-Bio1) were readjusted across replicates. For each replicate, an equal amount of protein was either directly trypsinized for the whole lysate assessment or subjected to incubation with streptavidin beads. Flow through was then collected and trypsinized. Both whole lysate and flow-through were labelled with TMT, pulled together and measured using LC-MS. The site occupancy of G3BP2 was then calculated for each replicates following the defined formula.



Extended Data Fig. 8. Sulfenylation of C73 modulates G3BP2 phase separation. (**a**) Schematic illustration of G3BP2 treatment used to prepare various cysteine modifications: PS-TNB, PSSH, PSH, and PS-IAM, PSOH and $PSO_{x=2,3}H$. DTNB: 5,5′-dithiobis(2-nitrobenzoic acid). IAM: iodoacetamide. (**b**) Representative microscopy images for G3BP2-Cy3 condensates (10 µM) formed under different cysteine modifications (PSH, PSOH, and PSO_xH) prepared as shown in (**a**). LLPS was induced using 50 ng/µl of total RNA extract. (**c**) Representative images of G3BP2-Cy3 condensates (10 µM) upon 30 min treatment with 20 µM IAM compared to not treated. Quantification of droplet area is shown below (n ≥ 3, independent preparation, one-way ANOVA, Tukey's HSD Test for multiple comparisons). Scale bar = 20 µm. (**d**) Representative images and quantification of FRAP assay performed in G3BP2-Cy3 pre-blocked with IAM and treated as for Figure 4e. (n ≥ 2 independent preparations, N ≥ 20 droplets analysed, two-way ANOVA, Sidak posthoc test, non-significant). (**e**) Annotated MS/MS spectra of G3BP2 peptides highlighting the BTD trapped cysteine 73 SOH upon arsenite treatment. (**f**) Changes in abundancy of G3BP2 C73-BTD peptide (depicted in (**e**)) in WT and *Cse*$^{-/-}$ MEFs treated or not with arsenite. (n = 2, two-way ANOVA, Fisher's LSD test). Error bars indicate SD. (**g**) Representative images of *in-cellulo* FRAP of GFP-G3BP2 in WT and *Cse*$^{-/-}$ MEFs. Quantification is shown in Figure 4j.



Extended data Fig. 9. PSOH/PSSH changes regulate G3BP2-mediated SG dynamics. (**a**) Representative gels for global PSOH and PSSH changes in MEF cells treated with 500 µM $NaAsO_2$ for 15 and 30 min. After 30 min $NaAsO_2$ was removed, and cells were allowed to recover for 30 min (recovery). BTD-labelling was used for PSOH, and the dimedone-switch method with DCP-Bio1 was used for PSSH. Quantification is shown in Figure 5a. (**b**) Representative western blot of G3BP2 sulfenylation and persulfidation upon the same treatment as in (**a**). Quantification is shown in Figure 5b. (**c**) Changes in G3BP2-persulfidation occupancy of C73 upon arsenite treatment and recovery in WT MEF. Untreated *Cse*$^{-/-}$ MEF was used for comparison. Site occupancy was calculated using sum of all cysteine peptides with different modifications. Absence of the value was considered as 0. Spectra of all identified peptides are shown in Supplementary figure 7. Error bars indicate SD. (**d**) Representative images of G3BP2-Cy3 condensates (10 µM) upon 30 min treatment with H_2S or DTNB. Quantification of droplet area is shown below (n ≥ 3, independent preparations, N> 550 droplets, one-way ANOVA, Tukey's HSD Test for multiple comparisons). Scale bar = 20 µm. (**e**) Representative images of G3BP2 condensates upon arsenite treatment and recovery in WT MEF. 15 min before recovery, cells were treated or not with 1 mM cocktail of H_2S production inhibitors (propargylglycine,PG and aminooxyacetic acid, AOAA), treatment was kept during recovery time (1 h). Quantification of SG number per cell is shown below (n = 3, several images per replicate, N > 700 cells, One-way ANOVA, Tukey's HSD Test for multiple comparisons. Error bars indicate standard error). Scale bar = 20 µm.



Extended data Fig. 10. H_2S donors dissolve SG in cells. (**a**) Representative images and (**b**) granule number per cells quantification of G3BP2 condensates upon 500 µM arsenite treatment and recovery (1h) in STHdhQ7 and STHdhQ111 cells. During recovery, cells were treated or not with 200 µM of GYY4137. N > 450 cells quantified, One-way ANOVA, Tukey's HSD Test for multiple comparisons. Errors bar represents standard error. (**c**) Representative images and (**d**) granule density per cells quantification of G3BP2 condensates upon 500 µM arsenite treatment and recovery (30 min) in WT and *Cse*$^{-/-}$ MEF. For the recovery, the cels were treated or not with 400 µM ergothioneine (ET). Ergothioneine has been shown to induce H_2S production in a CSE-dependent manner. N > 500 cells quantified, One-way ANOVA, Tukey's HSD Test for multiple comparisons.